UNIVERSITY OF
GOTHENBURG

Thesis for the Degree of Doctor of Philosophy

Double Inner-Shell Vacancies in Molecules

Author:
Dimitris Koulentianos

Supervised by:

Professor Raimund Feifel Dr. Marc Simon (DR)

Examiner:
Professor Dag Hanstorp

Opponent:
Professor Alexander Föhlisch

Department of Physics
University of Gothenburg

Sorbonne Université
Laboratoire de Chimie Physique -
Matière et Rayonnement

Doctoral Dissertations in Physics

Department of Physics
University of Gothenburg
412 96 Gothenburg, Sweden

Sorbonne Université
Laboratoire de Chimie Physique - Matière et Rayonnement
75005 Paris, France

April 29, 2019

©Dimitris Koulentianos, 2019
ISBN: 978-91-7833-488-9 (PRINT)
ISBN: 978-91-7833-489-6 (PDF)
URL: http://hdl.handle.net/2077/59862

Cover: Angular distributions of the ejected electrons during the formation of a double-core-hole pre-edge state, after the absorption of an X-ray photon (in black). In the direct channel (dipolar ionization-monopolar excitation) a p-wave emission takes place (red and blue parts), while the conjugate channel (dipolar excitation-monopolar ionization) will result in the emission of an s-wave (green part).

Printed by BrandFactory, Kållered, 2019

Typeset using LaTeX

To my family

Abstract

Molecular electronic states possessing a double core-vacancy, referred to as double-core-hole (DCH) states, were predicted more than thirty years ago, to have interesting properties, which would allow one to probe matter in a much more detailed way compared to conventional single core-vacancy techniques. Though DCH states are characterized by low cross-sections compared to the dominant single-core-hole (SCH) states, which implies experimental challenges, the development of third generation synchrotron radiation (SR) facilities and X-ray free electron lasers (XFEL), in combination with advanced spectroscopy techniques, resulted recently in a significant number of scientific works reporting on the observation of different types of DCH states.

Within the framework of this thesis, experimental work in terms of high resolution single channel electron spectroscopy was carried out, detecting DCH states of the form $K^{-1}L^{-1}V$, where one core electron has been ionized and the second has been excited to an unoccupied orbital V. One example concerns the case of HCl, where the experimental spectrum has been reproduced by a fit model taking into account Rydberg series within different spin-orbit multiplicities. From this analysis, the thresholds for the double ionization continua and the quantum defects for different Rydberg electrons have been extrapolated. Furthermore, electron spectra reflecting the formation of $K^{-2}V$ DCH states, which involve the K shells of the N and C atoms in CH_3CN, have also been recorded and interpreted based on a theoretical model considering the direct (dipolar ionization - monopolar excitation) or the conjugate (dipolar excitation - monopolar ionization) nature of each observed transition. In addition, the initial and final state effects contributing to the chemical shift between the two non-equivalent C atoms have been discussed and visualized by employing a Wagner plot.

Related results are reported on the formation of $K^{-2}V$ DCH states in SF_6 and CS_2. The influence of the slope of the potential energy curve on the broadening of the spectral features is discussed along with the appearance of a pronounced background. Fingerprints of nuclear dynamics upon the decay of several types of DCH states in H_2O have been identified by recording the related hyper-satellite Auger spectrum.

Complementary, the technique of multi-electron coincidence spectroscopy was used for the study of the formation of $K^{-2}V$ and K^{-2} DCH states in C_4H_{10}, where the latter type of DCHs with both core electrons being ejected to the continuum, has been measured directly and in the same experiment as the $K^{-2}V$ states.

Populärvetenskaplig sammanfattning

Den här avhandlingen bygger på studier av atomer och molekyler som växelverkar med ljus så att elektroner, med negativ laddning, slås ut från atomerna/molekylerna som blir positivt laddade joner. Effekten observerades av Heinrich Hertz år 1887 och förklarades teoretiskt med hjälp av den fotoelektriska lagen av Albert Einstein år 1905, som ledde till hans Nobelpris i Fysik. Einstein förklarade det som att energi överförs till materia i form av diskreta paket, fotoner, och att den (foto)elektron som slås ut får en rörelseenergi, E_k, som bestäms av $E_k = hv - E_b$, där E_b är fotoelektronens bindningsenergi hos atomen eller molekylen och hv är fotonens energi. I en atom eller molekyl kan elektronerna ockupera olika elektronskal, där elektroner från olika elektronskal har olika bindningsenergi. Beroende på fotonenergi kan man avlägsna elektroner från yttre (valens) elektronskal eller från ett inre (kärn) elektronskal. När en elektron avlägsnas från ett elektronskal så lämnas en vakans, som i sin tur kan starta flera andra processer.

Fotoelektronspektroskopi går ut på att mäta rörelseenergin hos de utslagna elektronerna, en teknisk utveckling som initierades med Kai Siegbahns banbrytande arbete som gav honom Nobelpriset i fysik 1981. Tack vare det systematiska arbete av Kai Siegbahn och hans forskargrupp vet vi idag att bindningsenergierna hos innerskalselektronerna kan ta olika värden beroende på deras kemiska omgivning. Detta fenomen är känt i litteraturen som kemiskt skift och ledde till begreppet elektronspektroskopi för kemisk analys (Electron Spectroscopy for Chemical Analysis (ESCA)), som flitigt används för att identifiera sammansättningen av molekyler eller fasta material. Även om Siegbahns teknik var revolutionerande på sin tid, så vet vi idag att ESCA-metodens känslighet är begränsad i vissa fall.

Redan för mer än 30 år sedan förutspåddes det, av Lorenz Cederbaum, att molekylära elektroniska tillstånd som involverar en dubbelinnerskalsvakans kommer att vara mera känslig för den kemiska omgivningen än enkelinnerskalsvakanser som i första hand studeras med Siegbahns ESCA metod.

Experimentella studier av tillstånd med två vakanser i inre skal har nyligen blivit möjliga tack vare utvecklingen av kraftfulla ljuskällor så som fri-elektron-laser (FEL) och synkrotronljuslagringsringar av tredje generationen, i kombination med högeffektiva och högupplösande elektronanalysatorer.

Tillstånd med dubbla vakanser i inre skal kan skapas på flera olika sätt, t.ex. genom att direkt frigöra båda elektronerna med en foton. Metoden som denna avhandling främst bygger på involverar mekanismer som påverkar två innerskalselektroner av vilka en frigörs samtidigt som den andra exciteras till ett tomt skal. Det finns två processer som leder till bildande av den

typen av dubbelvakanser i inre skal. I det ena fallet frigörs en av innerskalselektronerna i form av dipolär jonisering åtföljd av monopolär excitation av den andra innerskalselektronen; denna mekanism kallas för den direkta processen. Den andra mekanismen, som kallas för den konjungerade processen, bygger på en dipolär excitation av den ena innerskalselektronen som åtföljs av en monopolär jonisering av den andra innerskalselektronen. Målet med denna avhandling är att undersöka och kartlägga dessa dubbelvakanser i inre skal under användning av synkrotronljusstrålning och elektronspektrometrar av hög upplösning och hög insammlingseffekt i kombination med kvantkemiska beräkningar.

Résumé populaire en fraçais

L'observation de l'effet photoélectrique par H. Hertz en 1887 et son explication par A. Einstein en 1905 pour laquelle il a reçu le prix Nobel de physique constitue la base du développement de la technique de spectroscopie photoélectronique. L'idée derrière cette technique est de mesurer l'énergie cinétique du photoélectron, quand l'energie du photon est connue. Ensuite, l'équation $h\nu = E_b + KE$, ou $h\nu$ est l'énergie du photon et KE l'énergie cinétique du photoélectron, peut être utilisée pour obtenir l'énergie de liaison de l'électron E_b. En utilisant différentes énergies de photon, nous pouvons sonder depuis les couches de valence jusqu'aux couches profondes d'un atome ou d'un molécule.

Grâce au travail du physicien Kai Siegbahn, il a été observé que l'énergie du liaison d'un atome en couche K peut prendre différentes valeurs en fonction de son environnement chimique. Ce phénomène est connu sous le nom de déplacement chimique et il peut être utilisé pour identifier la composition d'un molécule. Ceci est connu sous le nom de spectroscopie électronique pour l'analyse chimique (Electron Spectroscopy for Chemical Analysis (ESCA)). Néanmoins, dans certains cas d'environnements chimiques similaires, il n'est plus possible de distinguer le même atome.

En 1986 il a été predit par L. Cederbaum que des états moléculaires ou deux atomes ayant un couche K ionisée, noté comme $K^{-1}K^{-1}$ seront plus sensibles à l'environnement chimique que les états K^{-1} étudiés au début de l'ESCA. Les états K^{-2}, ou deux électrons en couche K du même atome ont été éjectés sont intéressants à étudier en raison de la grande relaxation des orbitales moléculaires. En anglais ces états de double trous sont appelés "double-core-hole (DCH) states". La formation d'un état DCH peut être causé par un mécanisme où un électron K est ionisé et l'autre est excité. Ces états DCH sont notés comme $K^{-2}V$, ou V est l'orbitale moléculaire vide dans laquelle l'électron excité a été promu. Il y a deux manières de créer ces états $K^{-2}V$. Dans le chemin direct une ionisation dipolaire accompagnée d'une excitation monopolaire auront lieu. Dans le chemin conjugué, l'excitation dipolaire est accompagnée par une ionisation monopolaire. Les symétries des états $K^{-2}V$ sont interdites par spectroscopie d'absoprion conventionnelle, c'est pourquoi nous sommes intéressés à eux.

L'observation expérimentale des états K^{-2}, $K^{-2}V$, $K^{-1}K^{-1}$ et $K^{-1}K^{-1}V$ est devenue réalisable grâce au développement de laser à électrons libres (free electron laser (FEL)) et des centres de rayonnement synchrotron de troisième génération. Pour la détection des états $K^{-2}V$ et $K^{-1}K^{-1}V$ nous pouvons utiliser une configuration expérimentale à haute résolution avec un analyseur d'électrons. Pour la détection des états K^{-2} et $K^{-1}K^{-1}$, un spectromètre à bouteille magnétique peut être utilisé. Dans le cadre de cette thèse nous avons

étudié la formation des états $K^{-2}V$ de molécules en utilisant de rayonnement synchrotron à la ligne de lumière GALAXIES du synchrotron SOLEIL avec une configuration expérimentale à haute résolution.

Περίληψη στα ελληνικά

Η ανάπτυξη της Κβαντομηχανικής στις αρχές του προηγούμενου αιώνα είχε ως αποτέλεσμα την εις βάθος κατανόηση της ατομικής δομής. Χωρίς να εισέλθουμε σε λεπτομέρειες, είναι γνωστό ότι τα ηλεκτρόνια γύρω από τον πυρήνα ενός ατόμου μπορούν να κατανεμηθούν βάσει συγκεκριμένων κανόνων στα ατομικά τροχιακά, τα οποία είναι λύσεις της εξίσωσης Schrödinger για ένα άτομο. Ένα ατομικό τροχιακό περιγράφεται από τρεις κβαντικούς αριθμούς (n, ℓ, m_ℓ).

Ο κύριος κβαντικός αριθμός, $n = 1, 2, ...$, σχετίζεται με την ενέργεια[1] του ηλεκτρονίου στο άτομο, ενώ ο αζιμουθιακός και ο μαγνητικός κβαντικός αριθμός, $\ell = 0, ..., n-1$ και $m_\ell = -\ell, ..., 0, ..., \ell$ αντίστοιχα, σχετίζονται με την τροχιακή στροφορμή του ηλεκτρονίου. Ένα ηλεκτρόνιο περιγράφεται με βάσει τις τιμές των κβαντικών αριθμών του τροχιακού που καταλαμβάνει, καθώς επίσης και ενός τέταρτου κβαντικού αριθμού, $m_s = \pm 1/2$, ο οποίος δείχνει την τιμή της προβολής του σπιν του ηλεκτρονίου πάνω σε έναν άξονα. Στο σημείο αυτό οφείλουμε να αναφέρουμε ότι σύμφωνα με την απαγορευτική αρχή του Pauli, ένα ατομικό τροχιακό δεν μπορεί να καταλαμβάνεται από περισσότερα από δύο ηλεκτρόνια, και όταν καταλαμβάνεται από δύο ηλεκτρόνια, αυτά θα έχουν αντίθετες τιμές του κβαντικού αριθμού m_s.

Ηλεκτρόνια με την ίδια τιμή του κύριου κβαντικού αριθμού n, λέμε ότι καταλαμβάνουν την ίδια ηλεκτρονιακή στιβάδα. Ο φασματοσκοπικός συμβολισμός των στιβάδων ξεκινάει από το γράμμα K του λατινικού αλφάβητου, το οποίο αντιστοιχεί στην τιμή $n = 1$ του κύριου κβαντικού αριθμού. Ανάλογα για $n = 2$ έχουμε τη στιβάδα L κ.ο.κ. Το πλήθος των ηλεκτρονίων μιας στιβάδας δίνεται από τη σχέση $2n^2$, όπου n είναι ο κύριος κβαντικός αριθμός. Ηλεκτρόνια που καταλαμβάνουν τις στιβάδες K και L, αναφέρονται συνήθως ως ηλεκτρόνια κορμού ή εσωτερικά ηλεκτρόνια και είναι ισχυρά δέσμια καθώς «αισθάνονται» ολόκληρο ή «σχεδόν» ολόκληρο το θετικό πυρηνικό φορτίο. Αντίθετα τα ηλεκτρόνια των εξωτερικών στιβάδων, M,N, ..., «αισθάνονται» μόνο ένα μέρος του πυρηνικού φορτίου λόγω της θωράκισης από τα ηλεκτρόνια κορμού, είναι δηλαδή ασθενώς δέσμια και αναφέρονται ως ηλεκτρόνια σθένους. Τέλος αξίζει να αναφερθεί ότι ηλεκτρόνια μιας συγκεκριμένης στιβάδας καταλαμβάνουν διαφορετικές υποστιβάδες αυτής, το πλήθος των οποίων καθορίζεται από τις τιμές που παίρνει ο αζιμουθιακός κβαντικός αριθμός ℓ.

[1] Η ενέργεια του ηλεκτρονίου εξαρτάται από την τιμή του n μόνο στα υδρογονοειδή άτομα (άτομα που έχουν μόνο ένα ηλεκτρόνιο, π.χ. H, He^+), στα πολυηλεκτρονιακά άτομα (όλα τα άτομα εκτός από το υδρογόνο) η ενέργεια καθορίζεται από τις τιμές των n και ℓ.

Σύμφωνα με τα προαναφερθέντα, η στιβάδα K για την οποία $n = 1$, θα εχεί μία υποστιβάδα, $\ell = 0$, ενώ η στιβάδα L για την οποία $n = 2$, θα έχει δύο υποστιβάδες $\ell = 0, 1$. Όπως για τις στιβάδες, ανάλογα με την τιμή του ℓ, έχουμε τους ακόλουθους φασματοσκοπικούς συμβολισμούς, για $\ell = 0, 1, 2, 3$ έχουμε τις υποστιβάδες s,p,d,f αντίστοιχα. Οι διαφορετικές τιμές του m_ℓ αντιστοιχούν σε διαφορετικούς προσανατολισμούς των τροχιακών (π.χ. για $n = 2$ και $\ell = 1$ υπάρχουν τρία κάθετα μεταξύ τους τροχιακά 2p). Η κατανομή των ηλεκτρονίων στα τροχιακά γίνεται με βάση την αρχή της δόμησης, π.χ. για το άτομο του αργού (Ar) το οποίο έχει 18 ηλεκτρόνια θα έχουμε $1s^2 2s^2 2p^6 3s^2 3p^6$, όπου οι εκθέτες δηλώνουν τον αριθμό των ηλεκτρονίων σε κάθε στιβάδα και τις ανάλογες υποστιβάδες.

Πέρα από την ανάπτυξη της Κβαντομηχανικής, ένας ακόμα σημαντικός παράγοντας που αργότερα θα συνέβαλλε στην κατανόηση της δομής της ύλης ήταν η παρατήρηση του φωτοηλεκτρικού φαινομένου από τον H. Hertz το 1887 και η επεξήγηση του από τον A. Einstein το 1905, για την οποία του απονεμήθηκε το βραβείο Νόμπελ Φυσικής. Το φωτοηλεκτρικό φαινόμενο αναφέρεται στην εκπομπή ηλεκτρονίων από ένα σύστημα, όταν σε αυτό προσπίπτει φως. Η σημασία του φωτοηλεκτρικού φαινόμενου είναι μεγάλη, καθώς ανέδειξε το σωματιδιακό χαρακτήρα του φωτός και κατ' επέκταση τη διττή του φύση (σωματίδιο και κύμα). Έγινε δε η αφετηρία για την ανάπτυξη της πειραματικής τεχνικής που σήμερα ονομάζουμε *φωτοηλεκτρονιακή φασματοσκοπία*.

Η ιδέα πίσω από αυτήν την ευρέως διαδεδομένη πλέον τεχνική είναι η εξής: προκειμένου να αποσπαστεί ένα ηλεκτρόνιο, από το άτομο για παράδειγμα, που βρίσκεται δέσμιο (ιονισμός), πρέπει να αποκτήσει ενέργεια μεγαλύτερη ή τουλάχιστον ίση με την ενέργεια δέσμευσής του. Αυτή η ενέργεια του προσφέρεται από το απορροφούμενο φωτόνιο. Συνήθως η ενέργεια του φωτονίου είναι πολύ μεγαλύτερη από την ενέργεια δέσμευσης, με το πλεόνασμα ενέργειας να μετατρέπεται σε κινητική ενέργεια του εκπεμπόμενου ηλεκτρονίου. Λόγω της αρχής διατήρησης της ενέργειας θα είναι $h\nu = E_\delta + E_k$, όπου $h\nu$ είναι η ενέργεια του φωτονίου, E_δ η ενέργεια δέσμευσης του ηλεκτρονίου και E_k η κινητική του ενέργεια. Συνεπώς, γνωρίζοντας την ενέργεια του φωτονίου και μετρώντας την κινητική ενέργεια του ηλεκτρονίου μπορούμε να μετρήσουμε πειραματικά την ενέργεια δέσμευσης E_δ. Επίσης χρησιμοποιώντας φωτόνια διαφορετικών ενεργειών, μπορούμε να ιονίσουμε από τις εξωτερικές στιβάδες, μέχρι και τις εσωτερικές (K,L). Με τον τρόπο αυτό μπορούμε να έχουμε μια πολύ καλή εικόνα των ενεργειακών επιπέδων του υπό μελέτη συστήματος.

Η κατασκευή των κατάλληλων πειραματικών διατάξεων, είχε ως αποτέλεσμα τη συστηματική μέλετη πολλών ατομικών και μοριακών συστημάτων μέσω φασματοσκοπίας φωτοηλεκτρονίων, ενώ η ισχύς της αναδείχθηκε ιδιαίτερα μέσα από τη δουλειά του φυσικού Kai Siegbahn, ο οποίος παρατήρησε ότι η ενέργεια δέσμευσης των εσωτερικών ηλεκτρονίων (και πιο συγκεκριμένα αυτών της στιβάδας K) ενός ατόμου που συμμετέχει στο σχηματισμό ενός μορίου, παίρνει διαφορετικές τιμές ανάλογα με το περιβάλλον του στο μόριο (τα γειτονικά σε αυτό άτομα). Το φαινόμενο

αυτό είναι γνώστο ως *χημική μετατόπιση* και είναι η βάση της φασματοσκοπίας ηλεκτρονίων για χημική ανάλυση (Electron Spectroscopy for Chemical Analysis (ESCA)). Παρόλα αυτά, για περίπτωσεις όπου το ίδιο άτομο βρίσκεται σε παρόμοια περιβάλλοντα οι αντίστοιχες ενέργειες ιονισμού είναι πολύ κοντά μεταξύ τους και η προαναφερθείσα τεχνική δεν μπορεί πλέον να χρησιμοποιηθεί, όπως για την περίπτωση του άνθρακα στα μόρια C_2H_2, C_2H_4 και C_2H_6.

Πριν από τριανταπέντε περίπου χρόνια, μια θεωρητική μελέτη από τον L.S. Cederbaum κ.ά, έδειξε πως μοριακές καταστάσεις όπου δύο αντί για ένα εσωτερικά ηλεκτρόνια (από τη στιβάδα K) έχουν ιονιστεί, έχουν κάποιες πολύ ενδιαφέρουσες ιδιότητες. Πιο συγκεκριμένα, κατάστασεις όπου δυο διαφορετικά άτομα στο ίδιο μόριο, έχουν από μία ιονισμένη στιβάδα K (οι οποίες συμβολίζονται ως $K^{-1}K^{-1}$) θα χαρακτηρίζονται από αυξημένες χημικές μετατοπίσεις, επιτρέποντας έτσι να ξεχωρίσουμε το ίδιο άτομο σε παρόμοια περιβάλλοντα, όπως στο παράδειγμα που αναφέρθηκε παραπάνω, μετρώντας τις αντίστοιχες ενέργειες διπλού ιονισμού, οι οποίες θα διαφέρουν αρκετά μεταξύ τους. Η περίπτωση μιας διπλά ιονισμένης στιβάδας K (η οποία συμβολίζεται ως K^{-2}), παρουσιάζει επίσης ιδιαίτερο ενδιαφέρον λόγω της έντονης αναπροσαρμογής των τροχιακών σε αυτή την περίπτωση, καθώς αλλάζει η θωράκιση των ηλεκτρονίων σθένους. Στις προαναφερθείσες καταστάσεις έχει αποδοθεί ο αγγλικός όρος double-core-hole (DCH) states, ενώ ένας πιθανός όρος στα ελληνικά θα μπορούσε να είναι *διπλά εσωτερικά ιονισμένες* καταστάσεις. Οι συμβολισμοί $K^{-1}K^{-1}$ και K^{-2} (υπό την προϋπόθεση ότι έχουμε ιονισμένες στιβάδες K) μπορούν επίσης να χρησιμοποιηθούν για να αναφερόμαστε σε αυτές.

Πέρα από τις καταστάσεις K^{-2}, μια «κενή» στιβάδα K μπορεί να προκύψει μέσω ενός μηχανισμού ταυτόχρονου *εσωτερικού ιονισμού-εσωτερικής διέγερσης*. Κατά τη δημιουργία των καταστάσεων αυτών έχουμε τον ιονισμό ενός εκ των δύο ηλεκτρονίων της στιβάδας K, ενώ το δεύτερο μεταβαίνει σε ένα μη κατηλειμένο τροχιακό σθένους. Τέτοιες καταστάσεις που στα αγγλικά αναφέρονται ως DCH *pre-edge* states, θα μπορούσαν να αποδοθούν στα ελληνικά ως καταστάσεις *εσωτερικού ιονισμού-εσωτερικής διέγερσης*. Επίσης όπως έχει δειχθεί απο τον S. Carniato κ.ά υπάρχουν δύο πιθανοί «δρόμοι» που οδηγούν στη δημιουργία τους. Στην πρώτη περίπτωση η απορρόφηση ενός φωτονίου έχει ως αποτέλεσμα τον ηλεκτροδιπολικό ιονισμό ενός ηλεκτρονίου της στιβάδας K και την ταυτόχρονη μονοπολική μετάβαση ($\Delta\ell = 0$) του άλλου σε ένα μη κατειλημένο τροχιακό σθένους. Μεταβάσεις αυτής της μορφής ονομάζονται *άμεσες μεταβάσεις* (direct transitions). Αντίθετα, η απορρόφηση ενός φωτονίου μπορεί να έχει ως αποτέλεσμα την ηλεκτροδιπολική μετάβαση του πρώτου ηλεκτρονίου ($\Delta\ell = 1$) και τον ταυτόχρονο μονοπολικό ιονισμό του δεύτερου. Τέτοιες μεταβάσεις αναφέρονται ως *συζυγείς μεταβάσεις* (conjugate transitions). Για τις προηγούμες καταστάσεις έχει υιοθετηθεί ο συμβολισμός $K^{-2}V$, όπου το V αναφέρεται στο τροχιακό σθένους που καταλήγει το ένα εκ των δύο ηλεκτρονίων. Οι προαναφερθέντες μηχανισμοί εσωτερικού ιονισμού-εσωτερικής διέγερσης μπορούν να οδηγήσουν σε τελικές καταστάσεις οι οποίες είναι

απαγορευμένες μέσω φασματοσκοπίας απορρόφησης.

Η κατασκευή πειραματικών κέντρων ακτινοβολίας σύνγχροτρον (synchrotron radiation facility) τρίτης γενιάς καθώς και η ανάπτυξη του λέϊζερ ελευθέρων ηλεκτρονίων (free electron laser (FEL)), είχε ως αποτέλεσμα έναν σημαντικό αριθμό επιστημονικών δημοσιεύσεων, τόσο όσον αφορά τις καταστάσεις K^{-2} όσο και τις $K^{-2}V$. Οι πειραματικές τεχνικές για την ανίχνευση τέτοιων καταστάσεων βασίζονται είτε σε φασματοσκοπία υψηλής ευκρίνειας, χρησιμοποιώντας έναν ημισφαιρικό αναλυτή ηλεκτρονίων (ιδανική για την καταγραφή καταστάσεων $K^{-2}V$), είτε σε φασματοσκοπία χρόνου πτήσης (time-of-flight) χρησιμοποιώντας ένα φασματοσκόπιο μαγνητικής φιάλης (magnetic bottle spectrometer). Μια αναλυτική περιγραφή των παραπάνω είναι εκτός του σκοπού μιας εκλαϊκευμένης περίληψης, αλλά μπορεί να βρεθεί στο αγγλικό κείμενο αυτής της διδακτορικής διατριβής, το κύριο αντικείμενο της οποίας είναι η πειρματική μελέτη καταστάσεων $K^{-2}V$ με χρήση ακτινοβολίας σύνγχροτρον και των δύο προαναφερθέντων πειραματικών τεχνικών.

List of papers

This thesis is based on the following list of publications which are referred to in the text by their Roman numerals.

I. **KL double core hole pre-edge states of HCl**
D. Koulentianos, R. Püttner, G. Goldsztejn, T. Marchenko, O. Travnikova, L. Journel, R. Guillemin, D. Céolin, M.N. Piancastelli, M. Simon, and R. Feifel
Phys. Chem. Chem. Phys. **20**, 2724 (2018)

II. **Double-core-hole states in CH_3CN: Pre-edge structures and chemical-shift contributions**
D. Koulentianos, S. Carniato, R. Püttner, G. Goldsztejn, T. Marchenko, O. Travnikova, L. Journel, R. Guillemin, D. Céolin, M.L.M. Rocco, M.N. Piancastelli, R. Feifel, and M. Simon
J. Chem. Phys. **149**, 134313 (2018)

III. **Cationic double K-hole pre-edge states of CS_2 and SF_6**
R. Feifel, J.H.D. Eland, S. Carniato, P. Selles, R. Püttner, D. Koulentianos, T. Marchenko, L. Journel, R. Guillemin, G. Goldsztejn, O. Travnikova, I. Ismail, B. Cunha de Miranda, A.F. Lago, D. Céolin, P. Lablanquie, F. Penent, M.N. Piancastelli, and M. Simon
Sci. Rep. **7**, 13317 (2017)

IV. **Ultrafast nuclear dynamics in the doubly-core-ionized water molecule observed via Auger spectroscopy**
T. Marchenko, L. Inhester, G. Goldsztejn, O. Travnikova, L. Journel, R. Guillemin, I. Ismail, D. Koulentianos, D. Céolin, R. Püttner, M.N. Piancastelli, and M. Simon
Phys. Rev. A **98**, 063403 (2018)

V. **Formation and relaxation of K^{-2} and $K^{-2}V$ double-core-hole states in C_4H_{10}**
D. Koulentianos, R. Couto, J. Andersson, A. Hult Roos, R.J. Squibb, M. Wallner, J.H.D. Eland, M.N. Piancastelli, M. Simon, H. Ågren, and R. Feifel
In manuscript

The papers mentioned in the following list have not been included in the thesis.

- **Creation of O double K-shell vacancies through core-ionization core-excitation mechanisms in CO**
  D. Koulentianos, S. Carniato, R. Püttner, J.B. Martins, T. Marchenko, O. Travnikova, L. Journel, R. Guillemin, D. Céolin, M.N. Piancastelli, R. Feifel, and M. Simon
  In manuscript

- **Abundance of molecular triple ionization by double Auger decay**
  A. Hult Roos, J.H.D. Eland, J. Andersson, R.J. Squibb, D. Koulentianos, O. Talaee, and R. Feifel
  Sci. Rep. **8**, 16405 (2018)

- **Valence double ionization electron spectra of CH_3F, CH_3Cl and CH_3I**
  A. Hult Roos, J.H.D. Eland, D. Koulentianos, R.J. Squibb, L. Karlsson, and R. Feifel
  Chem. Phys. **491**, 42 (2017)

- **Auger decay of 4d inner-shell holes in atomic Hg leading to triple ionization**
  J. Andersson, R. Beerwerth, A. Hult Roos, R.J. Squibb, R. Singh, S. Zagorodskikh, O. Talaee, D. Koulentianos, J.H.D. Eland, S. Fritzsche, and R. Feifel
  Phys. Rev. A **96**, 012506 (2017)

- **Coulomb explosion of CD_3I induced by single photon deep inner-shell ionisation**
  M. Wallner, J.H.D. Eland, R.J. Squibb, J. Andersson, A. Hult Roos, R. Singh, O. Talaee, D. Koulentianos, M.N. Piancastelli, M. Simon, and R. Feifel
  In manuscript

Author's contributions to the papers

Paper I: Experimental work, data analysis, quantum chemical calculations and writing the main part of the paper

Paper II: Experimental work, data analysis and writing the main part of the paper

Paper III: Data analysis and commenting on the manuscript

Paper IV: Experimental work and commenting on the manuscript

Paper V: Experimental work, data analysis and writing the main part of the paper

Contents

List of Figures

Chapter 1

Introduction

Understanding atomic and molecular structure has been one of the main objectives of physics and chemistry for centuries. Over the years, many ideas have been proposed, which have later been refined or rejected. One of the first attempts to describe matter was performed by the ancient Greek philosophers Leucippus (Λεύκιππος) and his student Democritus (Δημόκριτος), around the fifth century B.C. They suggested that matter consists of fundamental units and the name given to each such unit was *atomo* (άτομο), meaning something that cannot be cut, from which we get the word "atom" used today. This atomic theory was abandoned until the early 1800s when John Dalton brought back the idea of atoms in order to explain why in chemical reactions there are always constant ratios of the reacting elements.

The development of quantum mechanics at the beginning of the previous century led to a deeper understanding of atomic structure and paved the way to describe the more complicated molecular structure. This, nowadays, fundamental physical theory was strongly guided by experimental results, imposing new models and refined perspectives on the currently existing ones. The Rutherford gold foil experiment [1] demonstrated that the Thomson model of the atom [2] was incorrect and the Rutherford model was introduced. The latter was refined by Bohr, leading to the Bohr model [3] of the atom. The shortcoming of the Bohr model to properly account for the poly-electronic atoms, in combination with the duality of matter (wave and particle) suggested by L. De Broglie [4], resulted in further refinements, and finally the Schrödinger equation [5], the corner-stone of modern, non-relativistic quantum mechanics came along. A function satisfying the Schrödinger equation of a given system is called the wavefunction of the system and allows one to obtain physical information related to the system. The atomic orbitals emerging from the solution [1] of the Schrödinger equation for an atom allow one to distribute the electrons of the atom in different shells and sub-shells and extract other physical information like the energies holding the electrons bound to them. Furthermore, the combination of atomic orbitals leads to the formation of more complex molecular orbitals, and thus the creation of molecules.

Another key factor in the understanding of matter was the explanation of the photoelectric effect, the ejection of electrons from the surface of a metal,

[1] An analytic solution of the Schrödinger equation is possible only for a very limited number of physical systems. The different approximative methods that can be applied in order to solve the Schrödinger equation for poly-electronic atoms or molecules, are the subject of quantum chemistry and are described in many textbooks [6].

after it had been irradiated by light, by A. Einstein in 1905 [7], a phenomenon first observed by H. Hertz in 1887 [8]. Einstein's work demonstrated the particle nature of light and provided clear evidence for its dual nature (wave and particle). Furthermore, it opened the way for the development of what is known today as *photoelectron spectroscopy*. The main idea behind this technique is to measure the kinetic energies of electrons ejected by photons of a known energy. Subsequently, conservation of energy implies that:

$$E_{\mathrm{K}} = h\nu - (E_{\mathrm{f}} - E_{\mathrm{i}}), \tag{1.1}$$

where E_{K} is the electron's kinetic energy, $h\nu$ the photon energy, E_{f} the final state energy of the sample and E_{i} the initial state energy of the sample before ionization. The quantity $(E_{\mathrm{f}} - E_{\mathrm{i}})$, which can be experimentally obtained, is called the binding energy and measures how strongly an electron is bound to the shell in its parent atom/molecule. By varying the photon energy, different shells can be probed and an overview of the electronic energy levels of the sample can be obtained.

The development of suitable experimental equipment during the 1960s [9, 10] made photoelectron spectroscopy one of the most important and powerful techniques for studies of atoms, molecules and solids. As demonstrated by K. Siegbahn [11], the binding energy of a core-shell electron of an atom can have different values when the atom is in different chemical environments. This phenomenon, known as chemical shift led to the well-known technique of electron spectroscopy for chemical analysis (ESCA). Nevertheless, in certain cases the chemical shifts are rather small, thus they make the distinction of the same atom in near-identical environments, very challenging.

Around the mid 1980s, theoretical investigations by Cederbaum and coworkers [12] suggested that states possessing a doubly ionized core-shell, referred to as double-core-hole (DCH) continuum states, would be characterized by some highly desirable properties. Specifically, DCH created by the ejection of two electrons occupying the core-shells of two different atoms in a molecule would result in enhanced chemical shifts, allowing for a more sensitive probe of the chemical environment, and improving in this way on the aforementioned weakness of conventional ESCA. Furthermore, in the same work [12] it was demonstrated that the creation of the vacancies on the same atomic site would result in large orbital relaxation effects. More recently, Carniato *et al.* [13, 14] demonstrated that DCH states formed through a core-ionization core-excitation mechanism could lead to final-state orbitals of different symmetries, forbidden in certain cases, in conventional near edge X-ray absorption fine structure (NEXAFS) spectroscopy, as well as to angular-distribution patterns for the ejected electron, different from those in conventional X-ray photoelectron spectroscopy (XPS). These latter DCH states are referred to as DCH pre-edge states and two mechanisms that lead to their formation have been proposed, namely the direct and the conjugate channel.

The elusive experimental observation of DCH states, though a first glimpse on them had already been reported in the late seventies by Ågren *et al.* [15], became more feasible thanks to the development of third-generation synchrotron radiation (SR) facilities and X-ray free electron lasers (XFEL) [16]. In

the first case the formation of a double core-vacancy relies on electron correlations, after the absorption of a single photon, while in the second case the ultra-short light pulses provided by an FEL, which are comparable with the lifetime of a single-core-hole (SCH) state, allow for the sequential absorption of two photons, which can be utilised for the formation of a DCH state. This thesis is focused on the experimental observation of molecular DCH states, formed after the absorption of single X-ray photons. The experimental data were acquired using SR sources and two different experimental techniques, namely high-resolution single-channel electron spectroscopy, using a hemispherical electron energy analyser, and time-of-flight (TOF) electron coincidence spectroscopy based on a magnetic bottle spectrometer.

The thesis is structured in the following way:

- In Chapter 2, a description of the fundamental concepts of atomic and molecular physics which are necessary for the understanding of the obtained results is given.
- In Chapter 3, the experimental techniques, along with the SR facilities where the experimental work was conducted, are discussed.
- In Chapter 4, the experimental results on DCH states, obtained within the framework of the thesis, are presented and a detailed explanation of them is given.
- Finally, in Chapter 5, the conclusions of the the thesis and further work that could be performed in the field of DCH spectroscopy are discussed, along with the potential applications that can emerge from the study of these states.

Chapter 2

Theoretical background

The aim of this chapter is to briefly describe the theoretical background of the processes that have been experimentally studied in this thesis. A comprehensive theoretical description can be found in several textbooks of quantum mechanics [17, 18] and physical chemistry [19]. The subjects to be discussed are the electronic structure of atoms and molecules, the processes of electronic excitation, and ionization and DCH states.

2.1 The structure of atoms

As mentioned in Chapter 1 of the thesis, in order to get a "picture" of how a poly-electronic atom looks like, one has to solve the Schrödinger equation. As an analytical solution is not possible for systems with several electrons, due to the interactions between the electrons, one can consider a hydrogenic atom (an atom with a single electron and an atomic number Z), find an analytic solution and then generalize the main ideas in order to describe the more complicated poly-electronic atoms.

If an one-electron system is considered, then the Schrödinger equation can be mathematically separated into a radial and an angular part. From the solution of the radial part, the principal quantum number n emerges, which takes the values $n = 1, 2, 3, ...$ and from the solution of the angular part one can obtain the azimuthal quantum number ℓ and the magnetic quantum number m_ℓ. For the azimuthal quantum number, it holds that $\ell = 0, 1, 2, ..., n-1$ and for the magnetic quantum number $m_\ell = -\ell, ..., 0, ..., \ell$. An atomic orbital is a wavefunction describing an electron in an atom and is defined by the three quantum numbers n, ℓ, m_ℓ. The value of the principal quantum number will determine the energy of the electron in the orbital through:

$$E_n = -\frac{Z^2 \cdot \mathrm{Ry}}{n^2}, \tag{2.1}$$

with the Rydberg unit Ry = -13.6 eV defined as $\mathrm{Ry} = hcR_\infty$, h being Planck's constant, c the speed of light in vacuum and R_∞ the Rydberg constant given by

$$R_\infty = \frac{m_\mu e^4}{8\epsilon_0^2 h^3 c}, \tag{2.2}$$

e being the electron charge, ϵ_0 the permittivity of vacuum and m_μ the reduced mass of the system, $m_\mu = m_e \cdot m_N / m_e + m_N$, with m_e the electron's mass and m_N the mass of the nucleus. As $m_N \gg m_e$, it is usually assumed that $m_\mu = m_e$.

The values of the azimuthal and the magnetic quantum numbers are related to the orbital angular momentum of the electron. More specifically the norm of the angular momentum for an electron having an azimuthal quantum number equal to ℓ will be $\sqrt{\ell(\ell+1)}\hbar$, with $\hbar = h/2\pi$, while the norm of the projection of the orbital angular momentum along an axis will be determined by the magnetic quantum number through $m_\ell \hbar$.

In order for a complete description of an electron in an atom, its spin state should also be included. As electrons are fermions, they have a semi-integer value of spin, $s = 1/2$, thus for the projection of the spin on one axis it will hold that $m_s = \pm 1/2$. The total wavefunction of the electron will be the product of its spatial wavefunction and its spin wavefunction. Furthermore, the Pauli principle states that fermions should be described by anti-symmetric wavefunctions, meaning that the sign of the total wavefunction should change when the labels of the particles are interchanged. This results in the Pauli exclusion principle stating that an atomic orbital can not be occupied by more than two electrons and when it is occupied by two electrons, they should have different m_s values. Thus an electron in an atomic orbital will be uniquely described by a wavefunction defined by the four quantum numbers n, ℓ, m_ℓ, m_s.

Electrons occupying orbitals with the same value of the principal quantum number are said to occupy the same shell, while electrons with the same value of the azimuthal quantum number are known to occupy the same sub-shell. Shells and sub-shells are usually noted with letters of the Roman alphabet according to their values. More specifically for shells it is K, L, M, N and continue accordingly for $n = 1, 2, 3, 4, ...$ respectively. For comparatively light atoms, the K and L shells are typically referred to as core/inner shells, while the other shells are referred to as the valence shells, noted with V. For sub-shells it is s (spherical), p (primary), d (diffused), f (fundamental) and then g, h, etc. for $\ell = 0, 1, 2, 3, ...$ respectively. From the above discussion about the maximum and minimal values of the quantum numbers and the Pauli exclusion principle, it can be shown that s orbitals can host at most two electrons, p orbitals six, d orbitals ten and f orbitals fourteen. Electrons are occupying the different shells and sub-shells of an atom according to the Aufbau (build-up) principle, in the energy order 1s 2s 2p 3s 3p 4s 3d 4p 5s 4d etc. For example, for a Ne atom with $Z = 10$, it will be $1s^2 2s^2 2p^6$.

Another aspect that should be addressed before concluding this brief discussion about the structure of an atom is the main difference in the energy levels of a poly-electronic and a hydrogenic atom. A degeneracy is present in the energy levels of the latter, meaning that an electron occupying different sub-shells within the same shell will have the same energy. The reason for that degeneracy can be found in the $1/r$ form of of the Coulomb potential felt by the electron of a hydrogenic atom. For of a poly-electronic atom, electrons do not feel a pure Coulomb potential anymore, but an effective potential resulting in the lift of the above mentioned degeneracy.

2.2 The structure of molecules

Molecules are formed when two or more atoms are brought close together. From a classical point of view the formation of a molecule can be seen as a balance between the attractive and the repulsive electrostatic forces felt by the electron clouds and the nuclei of the atoms, resulting in a structure having a lower energy than the sum of the energies of the different atoms involved.

From a quantum mechanical point of view, a very important approximation that can be applied in the description of a molecule is the Born-Oppenheimer approximation [20]. The main idea behind this concept is that as $m_p = 1836 \cdot m_e$, m_p being the mass of a proton and $m_N = A \cdot m_p$, A being the mass number of the nucleus, the nuclei are much heavier than the electrons. As a consequence, the velocity of the nuclei is much smaller than that of the electrons, thus the former can be considered stationary. Accordingly, on the timescale of the electron motion, the nuclear geometry can be considered as fixed in space and the Schrödinger equation can be solved only for the electrons. If one considers a diatomic molecule, the energy eigenvalues for the electronic part will depend on the internuclear distance R and a graph like the one shown in Figure 2.1 can be obtained.

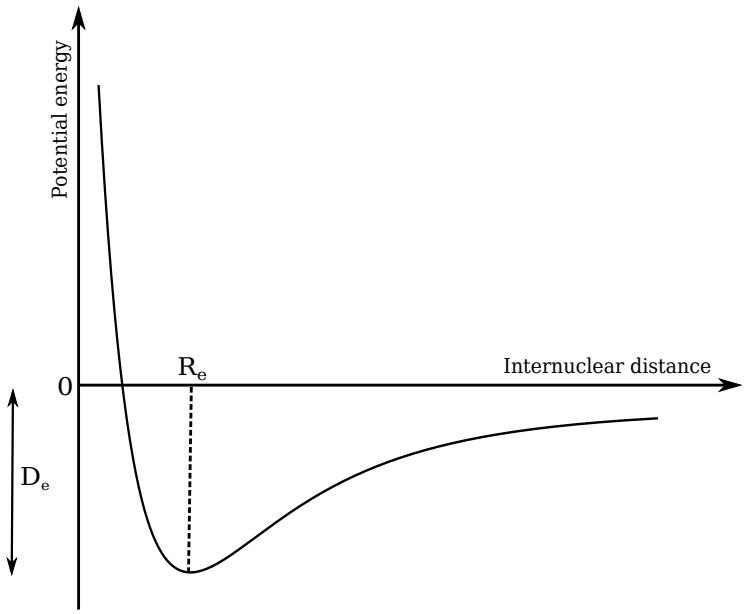

Figure 2.1: Potential energy curve for a bound state of a diatomic molecule. R_e located at the minimum of the curve stands for the equilibrium bond length, and D_e is the energy difference between the potential energy minimum and the dissociation limit.

The curve shown in Figure 2.1 is a potential energy curve (PEC), which has a minimum at a distance corresponding to the equilibrium bond length of the molecule R_e. The positive energies for short internuclear distances reflect the highly repulsive electrostatic forces at these distances, while the long-distance extreme of the curve corresponds to the limit of the isolated atoms. The energy corresponding to the equilibrium bond length is negative as expected.

For the case of a poly-atomic molecule, the same procedure can be applied but the calculations become more complicated as more parameters (distances, angles) have to be considered. The final result in this case is not a single curve but a surface, called a potential energy surface (PES).

For the description of the chemical bonding, two main theories have been suggested, namely the valence bond theory and the molecular orbital theory. The latter is the one widely used today and will be described shortly, nevertheless a brief description of valence bond theory [19] is worth mentioning, in order to introduce the fundamental concepts of σ and π bonds, which in turn are also used in molecular orbital theory. The main idea is that the formation of a chemical bond is based on the spin-pairing of the electrons occupying the valence orbitals of the involved atoms. If one considers two 1s orbitals, with one electron at each (as is the simple case of the H_2 molecule) then due to the spherical shape of the 1s orbitals a cylindrically shaped bond with respect to the internuclear axis will be created, called a σ bond. A σ bond can also be formed from the spin-pairing of an electron occupying a p orbital which is oriented along the internuclear axis with an electron occupying an s orbital. Concerning the spin-pairing of two electrons occupying a p orbital each, then depending on the relative orientations of the orbitals, two possible outcomes can emerge. If there is a side-by-side overlap, then the chemical bond formed will resemble a p orbital and is called a π bond. In contrast, if both p orbitals are oriented along the internuclear axis, then again the formation of a σ bond can occur. A characteristic example demonstrating the weaknesses of valence bond theory is the H_2O molecule. From the above mentioned argument one would expect an angle of 90° (as p orbitals are perpendicular to each other), in contrast to the experimentally found angle of 104.5° [19] of the molecule.

In the molecular orbital theory [18, 19], electrons are distributed in molecular orbitals, which are described by linear combinations of atomic orbitals (LCAO). This can be understood by considering again the case of a diatomic molecule AB. The wavefunction of a molecular orbital can be described as a linear combination of atomic orbitals, $\phi = c_A\chi_A + c_B\chi_B$, where χ_A, χ_B are the wavefunctions of the atomic orbitals and c_A, c_B pre-factors which have to be determined by calculations. For the case of a homonuclear diatomic molecule (i.e. A=B) one obtains $c_A = \pm c_B$ and in a simplified form one can use $\phi_\pm = \chi_A \pm \chi_B$. Considering the probability density $|\phi_\pm|^2$, it is straightforward to see that a term of the form $\pm 2\chi_A\chi_B$ emerges. This last term stems from the constructive/destructive interference of the atomic orbitals in the internuclear region and represents an enhancement/reduction of the probability density in this region. Thus, in the case of σ orbitals, occupation of ϕ_+ will favour the formation of a bond and for that reason is called a bonding orbital, whilst occupation of ϕ_- favours the dissociation of the molecule and for that reason it is called an anti-bonding orbital. The σ and π bonds discussed above can in turn be used to describe a σ or π molecular orbital (for the case of linear molecules), which could be either bonding or anti-bonding.

In general, simple arguments in terms of σ and π molecular orbitals can be employed to describe the electronic structure of diatomic molecules. For poly-atomic molecules, the molecular orbitals become more complicated and

a description considering only σ and π molecular orbitals can not necessarily be applied. Without going into details, we mention that group theory is necessary in this case to know the possible symmetries of the molecular orbitals, according to the point group that the molecule belongs to. A detailed description of group theory is beyond the scope of this thesis and for a description of it we refer the reader to Refs. [18, 19].

A final point before concluding this section on molecular structure is that beyond the electronic states of a molecule one has to consider its rotational and vibrational degrees of freedom as well. Molecular vibrations may give rise to asymmetries or substructures in the peaks appearing in a photoelectron spectrum and will be discussed in a separate section in the context of the Franck-Condon principle.

2.3 Ionized and excited states

In the ground state of an atom or a molecule, electrons populate the low energy orbitals. If the atom/molecule is irradiated by high energy photons, the energy of the absorbed photon can result in an electron being ejected to the continuum. High-energy photons (like hard X-ray radiation used in this thesis) are able to reach core shells and subsequently core electrons are ejected. This process, which is called core photo-ionization, is illustrated in the left panel of Figure 2.2, where the absorption of a high-energy photon leads to the ejection of a K-shell electron. Alternatively, the photon energy might be

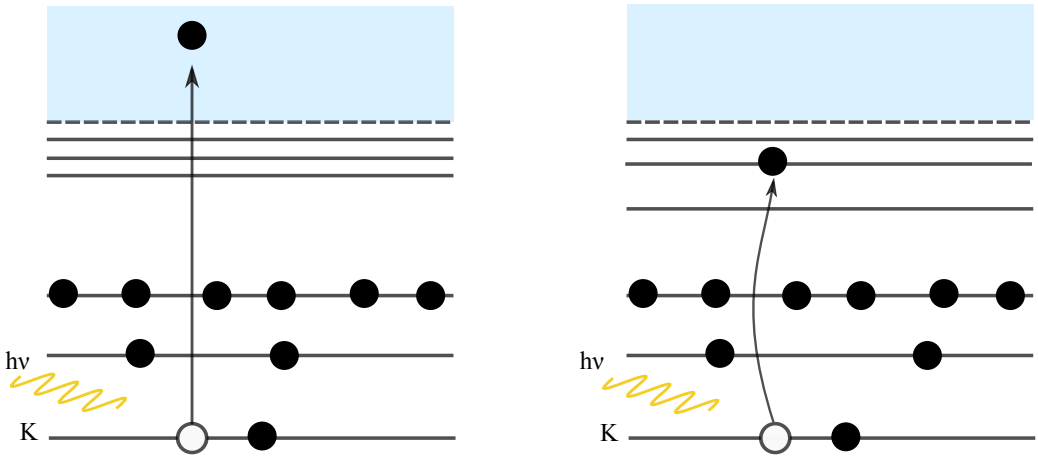

Figure 2.2: Absorption of a high energy photon can result in K shell ionization (left) or in a $K^{-1}V$ excitation (right).

sufficient to promote the electron from its orbital to an unoccupied valence orbital. This process is called excitation and can be seen in the right panel of Figure 2.2, for the case of a K-shell electron.

As mentioned in Chapter 1 of the thesis, in the case of photo-ionization the kinetic energy of the ejected photoelectron will be given by Eq. 1.1, where the quantity:

$$E_B = E^+ - E, \tag{2.3}$$

is called the electron binding energy. E^+ is the total energy of the cation and E the total ground-state energy of the sample. E_B can be written as a sum of two terms. The first term is associated with the energy required in order to remove an electron from its orbital. If, for simplicity, it is assumed that there is no change in the distributions of the other electrons, then this term is the orbital energy of the electron[1] ϵ [6, 18]. The second term in the binding energy is due to the charge flowing towards the hole after the ejection of the electron, which in turn screens the positive charge felt by the latter, causing it to accelerate. The measured electron kinetic energy will be higher and that will affect the measured binding energy as well. The previous process is called relaxation and can be taken into account in theoretical calculations of binding energies. Usually when performing photoelectron spectroscopy experiments one refers to the ionization potential (IP). If relaxation is ignored IP is equal to the negative orbital energy, IP=$-\epsilon$. This approximation is called Koopmans' theorem [21]. When relaxation is considered, the ionization potential can be expressed as [22, 23]:

$$\mathrm{IP} = -\epsilon - RC, \tag{2.4}$$

with RC being the relaxation-correlation energy; in this case it is IP=E_B.

Let us now discuss the excited states in a bit more detail. As conservation of energy implies, the energy of an excited state will be given by:

$$E^* = E + h\nu, \tag{2.5}$$

with E^* being the energy of the excited state and $h\nu$ the photon energy. Second, the matrix element for the transition from an initial state $|i\rangle$ to a final state $|f\rangle$ can be proven, using first order perturbation theory, to be given by [24] $\langle f|\, \hat{e} \cdot \vec{p} e^{i\vec{k}\cdot\vec{r}}\, |i\rangle$, with $\hat{e}$ being a unit verctor in the direction of the polarisation of the radiation field, $\vec{p}$ the momentum of the electron and $\vec{k}$ the wavevector of the field. This expression can be significantly simplified if one expands the exponential in Taylor series and keeps only the first term, $e^{i\vec{k}\cdot\vec{r}} \simeq 1$. From this approximation, known as the electric dipole approximation [24], and the commutation relation $[\vec{r}, H] = i\hbar\dot{\vec{r}}$, H being the Hamiltonian operator, it can be shown that the matrix element is given by the simplified expression [24]:

$$\langle f|\, \vec{D}\, |i\rangle\,, \tag{2.6}$$

with $\vec{D}$ being the electric dipole moment operator $\vec{D} = -e\vec{r}$ and e as in Section 2.1. For transitions of the form 2.6, the final states should satisfy for atomic orbitals the dipole selection rules:

$$\Delta\ell = \pm 1 \qquad \Delta m_\ell = 0, \pm 1. \tag{2.7}$$

Though the selection rules 2.7 are primarily describing atomic transitions, they can still be used in order to discuss the symmetries of the final states reached by the processes studied in molecular species. As we probe the K

[1] The orbital energy is the electron's energy in the field of the nucleus/nuclei and the *average* field of the other electrons and can be obtained from Hartree-Fock calculations.

shells of the molecular samples studied here, we expect them to retain an essentially pure atomic 1s character, meaning that a strong p character is expected for the final-state symmetry which can manifest either through a σ or a π final state orbital for the case of a linear molecule. For the case of non-linear poly-atomic molecules, group theory arguments can be used in order to check whether or not integrals of the form 2.6 vanish. Briefly, the initial state $|i\rangle$ in the expression 2.6 should correspond to the fully symmetric irreducible representation of the point group and one should consider transitions to final states of symmetries belonging to all the different irreducible representations of the point group.

If now the energy of the absorbed photon is much higher than the IP, then the excess of energy can simultaneously cause either the ejection of a second electron from a valence orbital to the continuum or the excitation of a valence shell electron to an unoccupied orbital. The first process is referred to as shake-off and the second as shake-up. Both processes are illustrated in Figure 2.3. An explanation for both processes can be found in the so-called

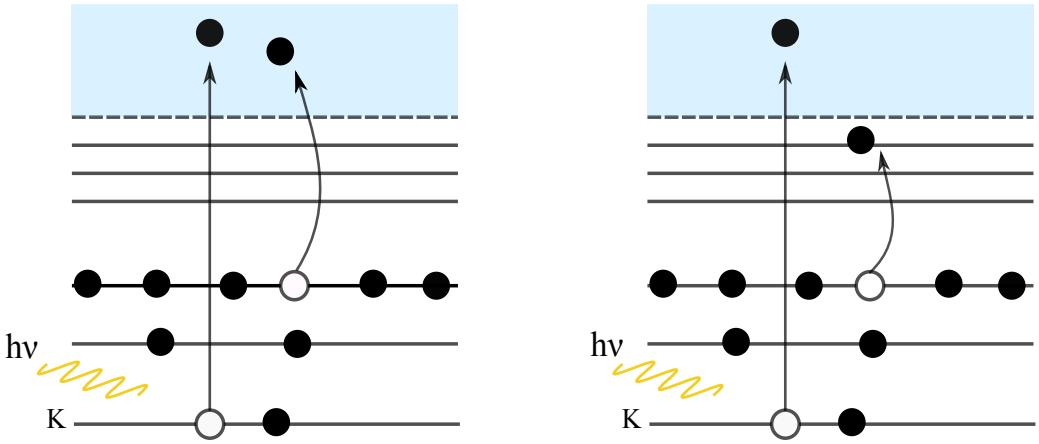

Figure 2.3: Core ionization might be accompanied by an ejection of a valence electron to the continuum, referred to as shake-off (left) or by an excitation of a valence electron to an unoccupied orbital, referred to as shake-up (right).

sudden approximation [17, 25]. As the photon energy greatly exceeds the IP, the ejected photoelectron will have a high kinetic energy meaning that it will leave the system very rapidly. In this way a system of $(N-1)$ electrons would still be described by a Hamiltonian corresponding to a system of N electrons. Subsequently, overlap integrals of the form $\langle\epsilon|i\rangle$ and $\langle f|i\rangle$ (corresponding to monopolar transitions), with $|\epsilon\rangle$ referring to the continuum wavefunction, would be non-vanishing, allowing in this way for the shake-off/shake-up processes described above. As will be discussed later in this chapter, some double-core-hole states can be considered being formed by super shake-off/shake-up processes where the ejection of a K-shell electron is accompanied by the simultaneous ejection/excitation of the second K-shell electron.

Before we conclude this section about ionized and excited states, it should be mentioned that there are two main decay pathways, which are depicted in

Figure 2.4 for the case of a core-ionized state. On the left-hand side of Figure 2.4 the Auger process is depicted, where the initial K shell vacancy is filled by an electron occupying a higher-energy orbital and the excess energy results in the ejection of a third electron to the continuum. In the present work focusing on holes in the K shell of fairly light atoms, the main decay channel is the KLL Auger decay (Figure 2.4) , where the first letter (K) refers to the shell where the initial vacancy has been created, the second letter (L) to the shell from which the electron that fills the vacancy departs and the third letter (L) to the shell in which the ejected Auger electron was initially bound. For an excited state, two possible processes have been observed. Either the excited electron participates in the Auger decay, a process referred to as participator Auger decay, or the excited electron remains in the valence orbital, while another electron fills the vacancy and an Auger electron is ejected, a process referred to as spectator Auger decay. In the right hand side of Figure 2.4, the alternative fluorescence process is shown, where an electron from a higher-energy orbital fills the core hole and a photon having an energy equal to the energy difference of the two shells is emitted. Usually for light elements ($Z < 20$) it has been found that Auger decay is the dominant decay path, after the creation of a K-shell vacancy, while fluorescence becomes more and more dominant for heavier elements ($Z > 20$).

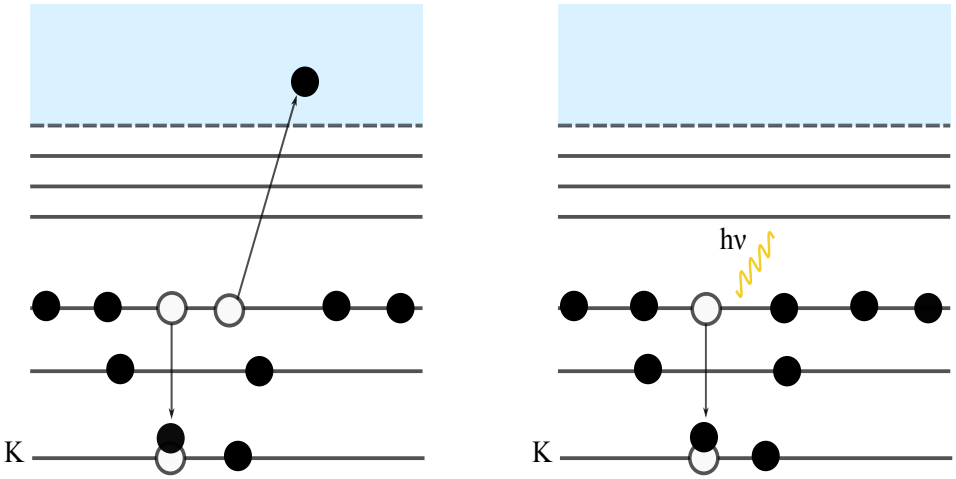

Figure 2.4: The Auger process (left), where a K-shell hole is filled by an L-shell electron, with the ejection of another L-shell electron to the continuum and the fluorescence process (right) where an L-shell electron fills the K-shell vacancy and a photon with energy equal to the energy difference of the two levels is emitted.

2.4 The Franck-Condon principle

As mentioned above, for the case of molecules one has to consider not only the electronic state in which the molecule can be, but also the nuclear motions within this electronic state. A way to illustrate the vibrational levels, for the

case of a diatomic molecule, is to plot a vibrational state as a straight line intersecting the potential energy curve in two points (classically considered as the turning points of the oscillator), as shown in Figure 2.5, where in total three

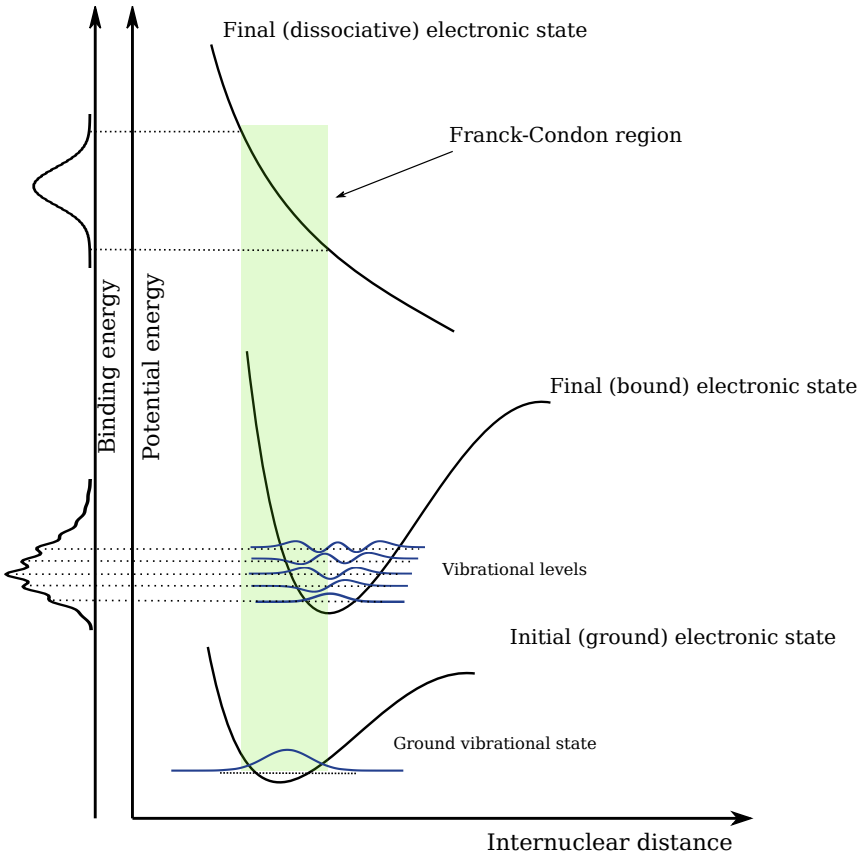

Figure 2.5: According to the Franck-Condon principle (for a diatomic molecule here), transitions take place only within the region defined by the initial geometry of the molecule. The shapes of the recorded photoelectron peaks reflect the nature of the final electronic state (bound or dissociative), as well as the overlap of the ground state vibrational wavefunction with the vibrational wavefunctions of the bound excited electronic state.

electronic states can be seen, the initial ground state, a final bound state and a final dissociative state. For the two first electronic states some vibrational levels are shown, along with the vibrational wavefunctions. In contrast, if the final electronic state of the molecule is dissociative, a continuum of levels with similar wavefunctions (described by an Airy function [26]) will emerge. This latter case will be further discussed in Section 4.7.

As the nuclei are much heavier than the electrons, the Franck-Condon principle [27, 28] states that, in a schematic representation, a transition between two different electronic states occurs "vertically", because electrons re-adjust much faster than the nuclei. In other words, one can imagine that during the electronic transition the initial separation of the nuclei remains unchanged, forming what is referred to as the Franck-Condon region, the vertical box shown in light green in Figure 2.5. Though the previous image is

based on classical arguments, it is very intuitive and stresses the importance of the Franck-Condon principle.

From a quantum mechanical point of view, this slow re-adjustment of the nuclei will be reflected in the shape of the ground state vibrational wavefunction, which should remain unchanged (described by a Gaussian function). Accordingly, the most intense transitions will be the ones for which the shape of the vibrational wavefunction of the electronically excited state resembles that of the ground vibrational wavefunction, as in this way the overlap that can be achieved is maximised [18, 19]. To illustrate this, we can consider transitions of the form 2.6, with $\vec{D}$ given under the Born-Oppenheimer approximation from:

$$\vec{D} = -e\sum_{n}\vec{r_n} + e\sum_{m=1}^{2} Z_m\vec{R_m}, \tag{2.8}$$

with n running over all electrons and m over the nuclei (two in this case). Z_1 and Z_2 are the atomic numbers of the two nuclei and $\vec{r_n}$, $\vec{R_m}$ are the position vectors of the electrons and nuclei, respectively. The final and initial state wavefunctions will be the products of the electronic and vibrational wavefunctions, $\left|\phi^f_{\text{el}}\phi^f_{\text{vib}}\right\rangle$ and $\left|\phi^i_{\text{el}}\phi^i_{\text{vib}}\right\rangle$, respectively. Substituting into 2.6 one obtains:

$$\begin{aligned} D_{fi} &= \left\langle \phi^f_{\text{el}}\phi^f_{\text{vib}}\right| \left(-e\sum_{n}\vec{r_n} + e\sum_{m=1}^{2} Z_m\vec{R_m}\right) \left|\phi^i_{\text{el}}\phi^i_{\text{vib}}\right\rangle \\ &= -e\sum_{n}\left\langle \phi^f_{\text{el}}\right| \vec{r_n} \left|\phi^i_{\text{el}}\right\rangle \left\langle \phi^f_{\text{vib}}\middle|\phi^i_{\text{vib}}\right\rangle + e\sum_{m=1}^{2} Z_m \left\langle \phi^f_{\text{el}}\middle|\phi^i_{\text{el}}\right\rangle \left\langle \phi^f_{\text{vib}}\right| \vec{R_m} \left|\phi^i_{\text{vib}}\right\rangle . \end{aligned} \tag{2.9}$$

For electronic transitions the second term on the right-hand side of 2.9 is equal to zero as the electronic states are orthogonal. The first term of 2.9 can be recognized as a dipole transition between two electronic states multiplied by the overlap integral of the vibrational states. Thus, larger overlaps of the vibrational states will result in more intense transitions, as the intensity is proportional to the Franck-Condon factors defined by:

$$\text{FC} = \left|\left\langle \phi^f_{\text{vib}}\middle|\phi^i_{\text{vib}}\right\rangle\right|^2. \tag{2.10}$$

The different overlaps between the ground-state vibrational wavefunction and the vibrational wavefunctions of the excited state will give rise to a vibrational progression which might be manifested through an asymmetry in the recorded photoelectron peak or some substructures as shown in Figure 2.5. One aspect that should be mentioned here is that as anti-bonding orbitals are occupied in excited states, the minimum of the potential energy curve will be found towards larger internuclear distances. As a consequence, in most cases a transition from the ground vibrational level of the ground electronic state to an excited vibrational level of the excited electronic state will be the most intense recorded experimentally. Note that these most intense transitions are

called vertical, while the adiabatic ones correspond to a transition between the ground vibrational levels of the two electronic states considered.

Finally, a transition from the electronic ground state to the final dissociative state, will manifest as a rather broad structure in the recorded electron spectrum. The shape of the peak can be understood by projecting each point of the ground vibrational wavefunction, in Figure 2.5, to the binding energy axis on the left through the repulsive potential energy curve. In this way it can be also shown that the broadening of the recorded peak will strongly depend on the slope of the repulsive potential energy curve. This is known as the Condon reflection approximation [29] and will be further discussed in Chapter 4, where the results of this thesis are presented.

2.5 Description of double-core-hole states

Double-core-hole (DCH) states are electronic states formed either by two core-shell electrons being ejected into the continuum, or by a core-ionization core-excitation process, or by a double core-excitation process. All processes can be seen in Figure 2.6, leading to a fully unoccupied, or hollow K-shell. The

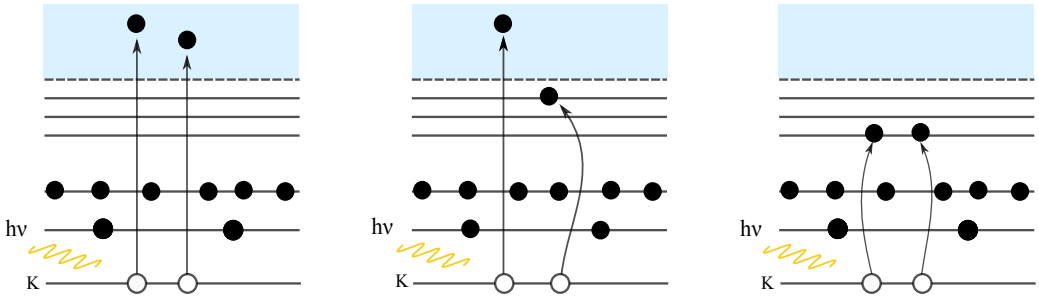

Figure 2.6: Formation of a continuum (K^{-2}) DCH state, with the emission of both K-electrons to the continuum (left), formation of a DCH pre-edge ($K^{-2}V$) state (middle), with the ejection of one K-electron to the continuum and excitation of the second K-electron to an unoccupied valence orbital, and formation of a neutrally excited DCH pre-edge ($K^{-2}V^2$) state, with the excitation of both K-electrons to an unoccupied valence orbital.

process depicted on the left-hand side of Figure 2.6 leads to what is known as a DCH continuum state, as both K-shell electrons end up in the continuum [30, 31], they are usually denoted as K^{-2} or $1s^{-2}$. The process in the middle of Figure 2.6 leads to the formation of a DCH pre-edge state [32, 33, 34], of the form $K^{-2}V$ or $1s^{-2}V$, with V denoting the final-state orbital, where the excited electron has been promoted to. Finally, the process on the right-hand side of Figure 2.6 leads to the formation of a neutrally excited DCH pre-edge state, denoted either $K^{-2}V^2$ or $1s^{-2}V^2$. This latter type of DCH states has not been experimentally observed yet.

As mentioned in Chapter 1, DCH continuum states were first discussed by Cederbaum *et al.* [12] in a seminal work published in 1986, where some of their unique properties were predicted. To begin with we mention that for the case

of molecules, two possible types of DCH can be formed. Either both vacancies will be created in the core shell of the same atom, or two different atoms of the same molecule might possess one core-vacancy each. The first type of DCH states is referred to as single-site (ss) DCH states while the latter as two-site (ts) DCH states. We note here that ts-DCH continuum states [35, 36] are usually denoted as $K^{-1}K^{-1}$, while ts-DCH pre-edge states as $K^{-1}K^{-1}V$. Both ss and ts DCH pre-edge states are shown in Figure 2.7, for the case of a diatomic molecule. As shown in Ref. [12] and further investigated in sub-

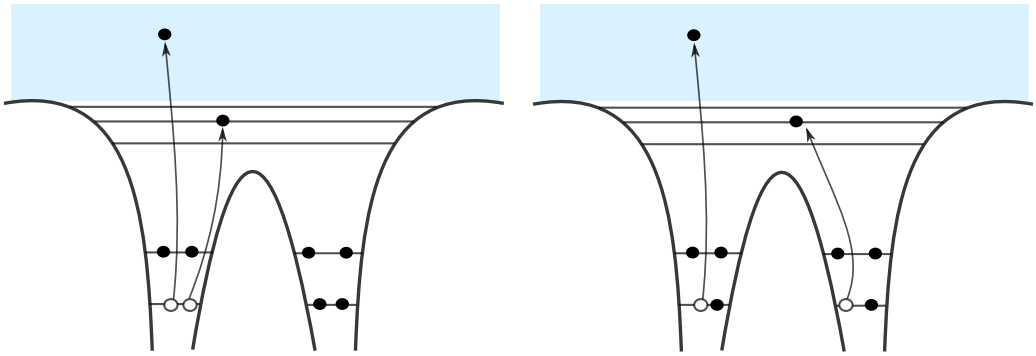

Figure 2.7: For the case of a (diatomic) molecule, both vacancies can be created on the same atomic site, leading to the formation of a ss-DCH state or on two different atomic sites, resulting in a ts-DCH state. Both ss and ts DCH states depicted here are of the pre-edge type.

sequent theoretical and experimental works [22, 23, 37], ss-DCH continuum states will exhibit large orbital relaxation effects and will allow for a separation between initial and final-state effects, while ts-DCH continuum states will be characterized by enhanced chemical shifts [36], making in this way DCH spectroscopy a potentially powerful tool for a detailed investigation of complex molecular systems [23].

These aspects become clearer from the equations that give the double-ionization potential (DIP) for ss and ts DCH continuum states. Before mentioning these equations, it should be noted, that for third-row or heavier elements not only the K shell is considered a core shell. As a consequence also DCH states with vacancies in different inner shells exist, like $K^{-1}L^{-1}$ in argon [33]. In the following we shall restrict the discussion for reasons of simplicity to two holes in the K shell, i.e. K^{-2} or $K^{-1}K^{-1}$ states. Following Refs. [22, 23] and in analogy with equation 2.4, we have:

$$\mathrm{DIP} = -\epsilon_A - \epsilon_B - RC(A^{-1}, B^{-1}) + \mathrm{RE}(A^{-1}, B^{-1}), \tag{2.11}$$

with ϵ_A, ϵ_B the orbital energies of the core-shell electrons of atoms A, B respectively, $\mathrm{RE}(A^{-1}, B^{-1})$ the Coulomb repulsion energy between the two core holes and $\mathrm{RC}(A^{-1}, B^{-1})$ the generalized relaxation-correlation energy, given by:

$$RC(A^{-1}, B^{-1}) = RC(A^{-1}) + RC(B^{-1}) + NRC(A^{-1}, B^{-1}), \tag{2.12}$$

with $RC(A^{-1})$, $RC(B^{-1})$ as in equation 2.4 and $NRC(A^{-1}, B^{-1})$ the non-additive contribution in the relaxation energy of a DCH state. For the case of a ss-DCH continuum state i.e. A=B, $NRC(A^{-1}, B^{-1})$ is called the excess generalized energy, denoted as $ERC(A^{-2})$ and we obtain from equations 2.11, 2.12:

$$\mathrm{DIP_{ss}} = -2\epsilon_A - 2RC(A^{-1}) - ERC(A^{-2}) + RE(A^{-2}). \tag{2.13}$$

Subtracting equation 2.4 from equation 2.13 gives:

$$\mathrm{DIP_{ss}} - \mathrm{IP} = \mathrm{IP} - ERC(A^{-2}) + RE(A^{-2}). \tag{2.14}$$

As both $\mathrm{DIP_{ss}}$ and IP can be measured experimentally, $ERC(A^{-2})$ can be obtained, given that the Coulomb integral for a K-shell is given by the formula [22, 23]:

$$RE(A^{-2}) = \left(\frac{2^{5/2}}{3\pi}\right)(Z - 2^{-3/2}). \tag{2.15}$$

Finally it holds that:

$$RC(A^{-2}) = ERC(A^{-2}) + 2RC(A^{-1}), \tag{2.16}$$

and from second-order perturbation theory, by neglecting correlation [22, 23], we have $ERC(A^{-2}) = 2RC(A^{-1})$, so that:

$$RC(A^{-2}) = 4RC(A^{-1}). \tag{2.17}$$

Thus $RC(A^{-1})$, which is a final-state effect can be estimated separately from the orbital energy ϵ_A, an initial-state effect. It should be noted that this separation is not possible by conventional SCH spectroscopy, as pointed out in Ref. [37].

For the case of ts-DCH continuum states, the non-additive term in equation 2.12 is called the inter-atomic generalized relaxation energy, denoted as $IRC(A^{-1}, B^{-1})$ and from equation 2.11, it will be for the ts DIP:

$$\begin{aligned}\mathrm{DIP_{ts}} = &-\epsilon_A - \epsilon_B - RC(A^{-1}) - RC(B^{-1}) \\ &-IRC(A^{-1}, B^{-1}) + RE(A^{-1}, B^{-1}).\end{aligned} \tag{2.18}$$

Considering the IP formula 2.4, for a core hole at site A and a core hole at site B, and subtracting both from equation 2.18, with $RE(A^{-1}, B^{-1}) = 1/r$, r being the distance between the two core vacancies, we obtain:

$$\mathrm{DIP_{ts}} - (\mathrm{IP}(A^{-1}) + \mathrm{IP}(B^{-1})) = -IRC(A^{-1}, B^{-1}) + 1/r. \tag{2.19}$$

With equation 2.19 in mind, let us now consider the C_2H_{2n} ($n = 1, 2, 3$) series studied theoretically in the initial DCH work by Cederbaum *et al.* [12]. As the values of the C K-shell IP are almost the same for all three cases [22] one can immediately see the influence of the environment in the measured ts DIP value through the $1/r$ factor on the right-hand side of equation 2.19. The repulsion energy will be the highest for the triply bonded C_2H_2 as the distance between the two C atoms is the shortest, while the value of $IRC(A^{-1}, B^{-1})$ has

been found to be positive for all three cases [22]. All the information for the relaxation process is contained in the value of $IRC(A^{-1}, B^{-1})$. More specifically, a positive value of IRC means that the vacancies are close to each other, as a vacancy at the atomic site A will attract charge towards it, but at the same time the relaxation of the vacancy at the atomic site B will be enhanced. In contrast, a negative value of IRC will indicate an enhancement of the electron density on the vicinity of one vacancy and a lack of it on the vicinity of the second, thus the two vacancies should be further apart in this case [22, 23].

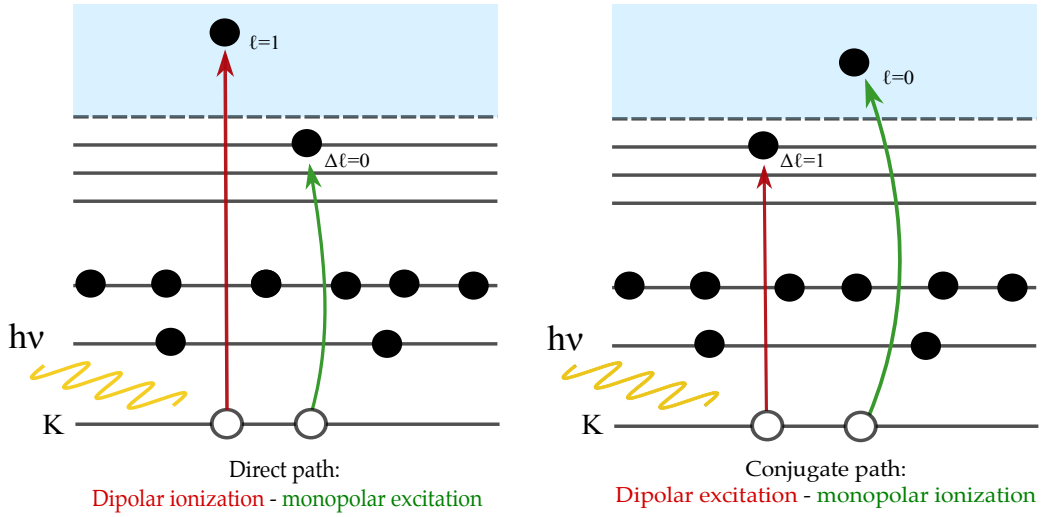

Figure 2.8: In the direct channel (left), absorption of a single photon leads to the dipolar ionization of the first K-electron accompanied by a simultaneous monopolar shake-up of the second K-electron. In the conjugate channel (right) single-photon absorption leads to the dipolar excitation of the first K-electron, accompanied by monopolar shake-off of the second K-electron.

So far, we have discussed what a DCH state is, as well as their different types and we have considered their potential applications from the properties they possess. We shall now attempt a description of the mechanisms leading to the formation of a DCH state. Let us start from the formation of ss-DCH continuum states. In this case, the sudden approximation is manifested though a super shake-off mechanism, and will cause the ejection of the second K-electron to the continuum. As mentioned in Section 2.3, the manifestation of the sudden approximation will strongly depend on the photon energy used to trigger the formation of a DCH state. In most cases, shake processes are fully developed when the excess energy of the photoelectron is equal to the binding energy [38]. For lower photon energies, a knock-out mechanism manifests, where the outgoing K-electron "knocks out" the second K-electron.

In what concerns ss-DCH pre-edge states, things become a bit more complicated as two mechanisms have to be considered according to Carniato *et al.* [13, 14], namely the direct and the conjugate pathway. A shake-up (shake-off) contribution is present for the direct (conjugate) channel in analogy with

the valence shake processes described originally by Martin and Shirley [39]. In the case of the direct path, single-photon absorption leads to the dipolar ionization of the first K-electron, with the second K-electron being excited by a monopolar shake-up process. Alternatively, single-photon absorption can lead to the dipolar excitation of the first K-electron, with the second K-electron being ejected to the continuum by a monopolar shake-off process, which is referred to as the conjugate path [32, 34]. Both the direct and the conjugate pathways are illustrated in Figure 2.8. It should be noted here, that for the case of argon in Ref. [33], knock contributions were theoretically predicted by Yarzhemsky and Amusia [40], and thought they did not become evident from the data analysis, nevertheless they can not be excluded.

Regarding the formation of ts-DCH states, according to recent works [35, 36], the main mechanism that has been suggested is knock-out/knock-up, where after the absorption of a single photon, the K-electron departing from one atomic site collides with the K-electron in a second atomic site leading in this way to the formation of a ts-DCH continuum/pre-edge state.

Chapter 3

Experimental techniques

In this chapter the experimental techniques and light sources used to obtain the results presented in this thesis are described. All the results were obtained by performing synchrotron radiation experiments, using primarily high resolution single-electron spectroscopy. Additional results were obtained by means of time-of-flight multi-electron coincidence spectroscopy. The beamline where the main part of the experimental work was conducted, the **G**reat be**A**m**L**ine for **A**dvanced **X**-ray **I**nelastic scattering and **E**lectron **S**pectroscopy (GALAXIES) of **S**ource **O**ptimisée de **L**umiére d' **E**nergie **I**ntermédiaire du **L**URE (SOLEIL), will also be briefly described. Finally an overview of time-of-flight electron spectroscopy using a magnetic bottle will be given.

3.1 Synchrotron radiation

Synchrotron radiation is the electromagnetic radiation emitted by charged relativistic particles when they are accelerated, such as is the case for an electron traversing a magnetic field perpendicular to its direction of motion. The charged particles are usually electrons and to manipulate them in a controlled fashion, three common magnetic structures are used: a bending magnet, a wiggler or an undulator. Synchrotron radiation produced at bending magnets was utilised in first generation synchrotron radiation facilities. Today, wigglers and more commonly undulators are used in modern third-generation synchrotron radiation facilities. Though undulators and wigglers seem to be quite similar in terms of their magnet arrangements, they emit light with quite different characteristics [41]. We shall now briefly discuss an undulator and mention what distinguishes it from a wiggler.

An undulator is a periodic magnetic structure, as shown in Fig. 3.1. It consists of a series of magnets of alternating polarity (N-S, S-N) placed next to each other, and it is characterized by a moderate magnetic field strength, resulting in some highly desirable properties. The magnetic period of the undulator is denoted λ_u. As electrons enter the undulator, they undergo small excursions, also known as undulations, from their trajectory due to the presence of the magnetic field. In each of these undulations, the electrons are centripetally accelerated, and thus emit synchrotron radiation. As shown in Fig. 3.1, the emission of radiation is tangential to the electron's trajectory. The narrow-cone radiation pattern results from the relativistic transformation

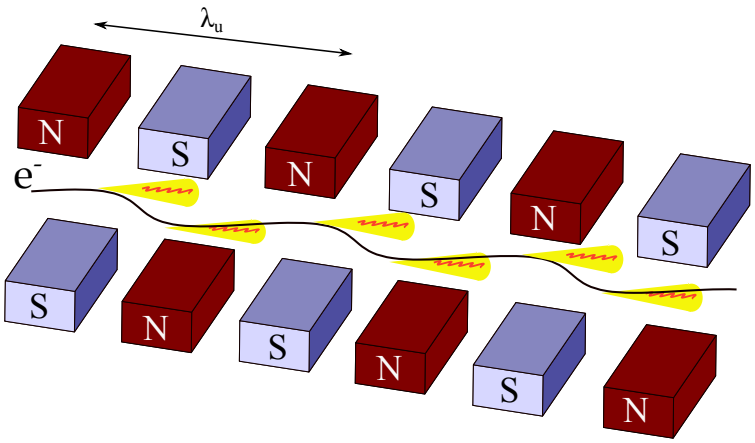

Figure 3.1: An electron traversing an undulator will emit light at the turning points in a form of a narrow radiation cone, as seen by an observer in the reference frame of the laboratory.

from the reference frame moving with the oscillating electron to the reference frame of the laboratory [41].

The wavelength of the emitted radiation is given by the undulator equation [41]:

$$\lambda = \frac{\lambda_u}{2\gamma^2}(1 + \frac{K^2}{2} + \gamma^2\theta^2), \tag{3.1}$$

where $\gamma = 1/\sqrt{1 - v^2/c^2}$ is the Lorentz factor, with v being the velocity of the electrons, θ standing for the emission angle of the observed radiation and K, given by the formula:

$$K = \frac{eB_0\lambda_u}{2\pi m_e c}, \tag{3.2}$$

being the deflection parameter and having a value $K \leq 1$ for the case of an undulator and $K \gg 1$ for a wiggler. Here B_0 is the strength of the magnetic field, m_e the electron mass and c the speed of light in vacuum. As a result of the moderate magnetic field strength of an undulator, interference effects take place resulting in narrow bandwidths and radiation cones.

From equation 3.1 it can be seen that the wavelength of the emitted light is determined by the deflection parameter, as B_0 can be changed by moving closer or bringing apart the magnetic arrays (jaws) of the undulator. Today's synchrotron radiation facilities typically cover a wavelength range from EUV to hard X-rays. The undulator supplying the GALAXIES beamline of the French national synchrotron radiation facility SOLEIL, can deliver light in the tender to hard X-ray (2.3 - 12 keV) range.

3.2 SOLEIL Synchrotron radiation facility and the GALAXIES beamline

The main part of the experimental work of this thesis was conducted at the GALAXIES beamline of the synchrotron radiation facility SOLEIL, located

in Saint-Aubin, France. SOLEIL is a third-generation synchrotron radiation facility, inaugurated in 2006 and delivers synchrotron radiation from far infrared to hard X-rays. A schematic representation can be seen in Fig. 3.2.

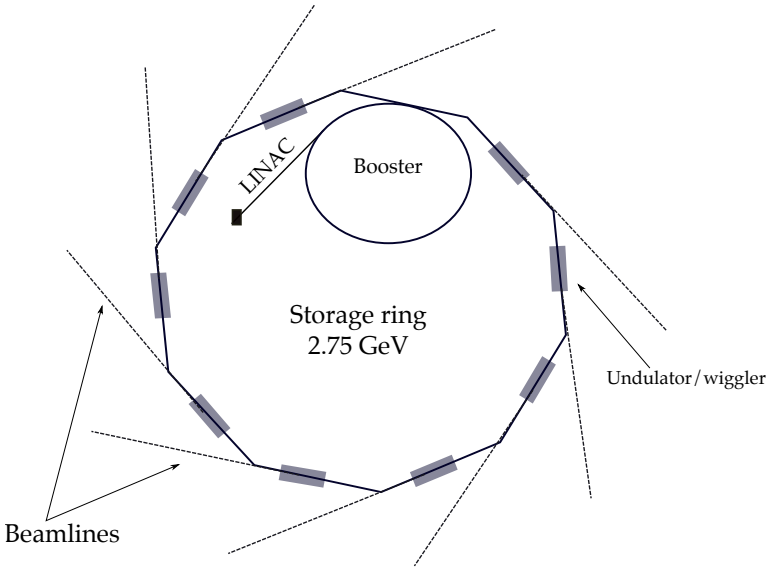

Figure 3.2: Schematic representation of a third-generation synchrotron radiation facility like SOLEIL.

Electrons emitted from the surface of a metal cathode enter the linear accelerator (LINAC), before moving to the booster where they are further accelerated, reaching in the case of SOLEIL an energy of 2.75 GeV, which is the energy they retain once transferred to the storage ring. As the electrons orbit in the storage ring, they traverse the bending magnets and undulators / wigglers, emitting radiation which serves the experimental purposes at the different beamlines. In order to restore the electrons' energy after the emission of light, a radiofrequency accelerating cavity (not shown in Figure 3.2) is used.

The light emitted by the electrons traversing the undulator of the GALAXIES beamline [42] can be in tender to hard X-ray range, thus the beamline is suited to study processes involving the K shells of comparatively heavy atomic and molecular systems. The beamline comprises two experimental end-stations, one for performing resonant inelastic X-ray scattering (RIXS) measurements and the other dedicated to hard X-ray photoelectron spectroscopy (HAXPES). The latter was used for obtaining the results of this thesis. A schematic of the beamline, taken from Ref. [43], is displayed in Figure 3.3. The beamline is equipped with an in-vacuum 20 mm period undulator U20, having 98 periods [42]. A double Si(111) crystal monochromator (DCM) is used to select the desired photon energy. Furthermore a four-bounce, non-dispersive, high-resolution monochromator (HRM) can be employed, which will further narrow the photon energy bandwidth to about $\simeq$100 meV. The DCM is followed by a collimating spherical mirror (M1) the coating of which can be either carbon for low photon energies (2.3 - 6 keV) or palladium for higher photon energies (6 - 12 keV). A quarter wave plate (QWP) installed between

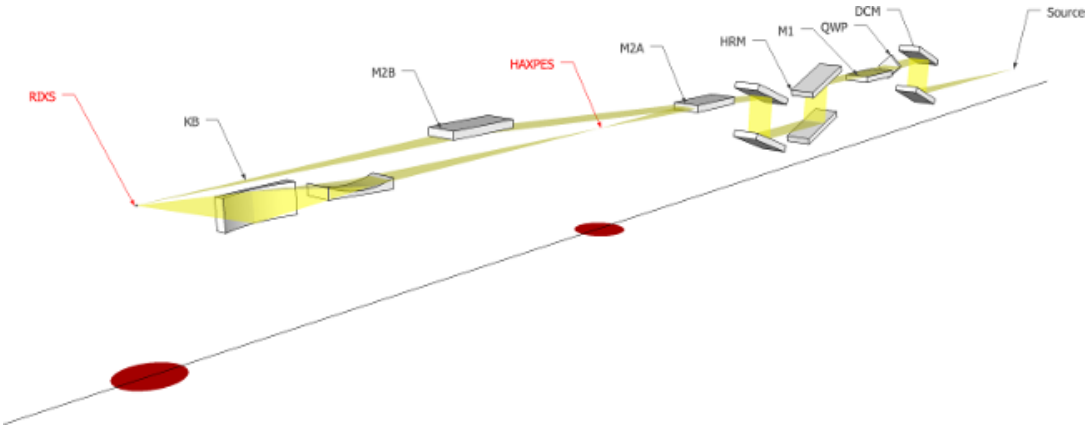

Figure 3.3: An overview of the GALAXIES beamline located at SOLEIL [43].

the source and M1 can be used in the case that vertically polarized light is necessary for the experiment. Finally, the beam is focused into the HAXPES end-station by using the M2A toroidal mirror, the coating of which is also palladium. A description of the RIXS end-station is beyond the scope of the thesis, but may be found in Ref. [42]. In the next section a detailed description of the HAXPES setup is given.

3.3 HAXPES setup

High-resolution single-electron spectroscopy is an indispensable tool in detecting the processes studied in this thesis. An overview of the setup used for that purpose, installed in the HAXPES end-station [44] of the GALAXIES beamline of SOLEIL is shown in Figure 3.4. In this setup, linearly polarized X-rays are used to ionize the sample enclosed in a gas cell. The ejected photoelectrons are then collected by the electrostatic lens of a VGScienta EW4000 hemispherical electron analyser, the axis of which is set parallel to the polarization direction of the incoming radiation. A special characteristic of the analyser lens is its wide-angle opening, which can be chosen to be either 45° or 60°. This feature is of special importance, as the wide opening of the lens can compensate for the weak cross-sections of the processes studied here, by allowing more electrons to be collected.

A key experimental parameter in the HAXPES setup is the pass energy E_p of the electron analyser. The kinetic energy of an electron is reduced to the value of the selected pass energy, by the lens system, prior to entering the analyser. This retardation is achieved by applying a potential, the value of which is defined by the electron kinetic energy, at which the processes we are interested in will manifest. For example, if we want to collect electrons with a kinetic energy around 2500 eV and the selected pass energy is 500 eV, then a retarding potential of 2000 eV will be applied. The value of the retarding potential will increase in increments by a step size selected by the experimenter, in order to scan a kinetic energy region.

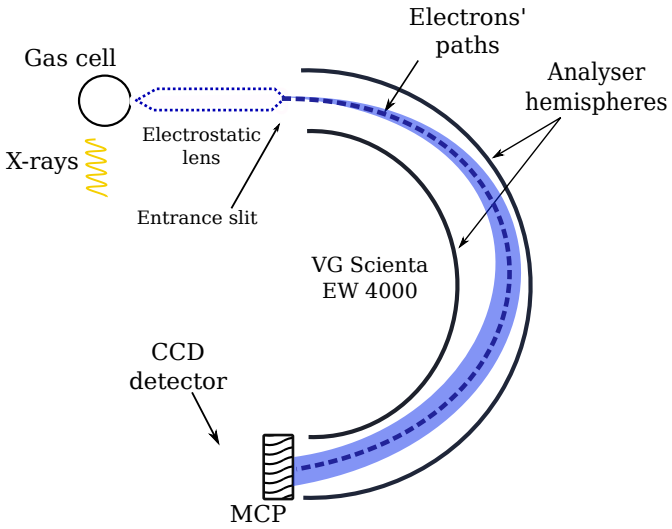

Figure 3.4: After the sample enclosed in a gas cell has been irradiated with X-rays, electrons are collected by a hemispherical electron energy analyser. Only those electrons having a kinetic energy close to the set pass energy of the analyser will pass through and be recorded. In this way a process can be studied at high energy resolution.

After the electrons pass through and get focused by the lens they enter into the region in between the two concentric hemispheres of the analyser, the latter being kept at a constant voltage. Within the hemispherical shells the electrons are dispersed according to their kinetic energies. In general, the dispersion of an electron entering the analyser depends on its kinetic energy and the angle it enters the analyser [45]. Assuming an electron enters the analyser with kinetic energy equal to the set pass energy, and its velocity parallel to the axis of the electrostatic lens. This electron will traverse the analyser at a constant radius in-between the radii of the hemispheres, exit the analyser and hit the detector. As the radius of an electron's trajectory in the analyser significantly depends on the pass energy, only electrons that have a kinetic energy close to the set pass energy will exit the analyser. Electrons with kinetic energies much lower or higher than E_p will hit the analyser hemispheres and will not reach the detector. In this way, processes taking place in a certain kinetic energy range can be probed with great accuracy.

The energy resolution of the analyser of the HAXPES end-station depends on the selected pass energy, as well as on the width of the analyser slit. Based on Ref. [46], the resolution can be approximated by:

$$\Delta E = E_p \cdot \frac{S}{2R_0}, \tag{3.3}$$

with E_p being the pass energy as before, S the width of the slit and R_0 the main radius of the analyser (the one exactly in-between the radii of the concentric shells). As can be seen from equation 3.3, decreasing the pass energy and the slit width will result in an enhanced energy resolution. The drawback

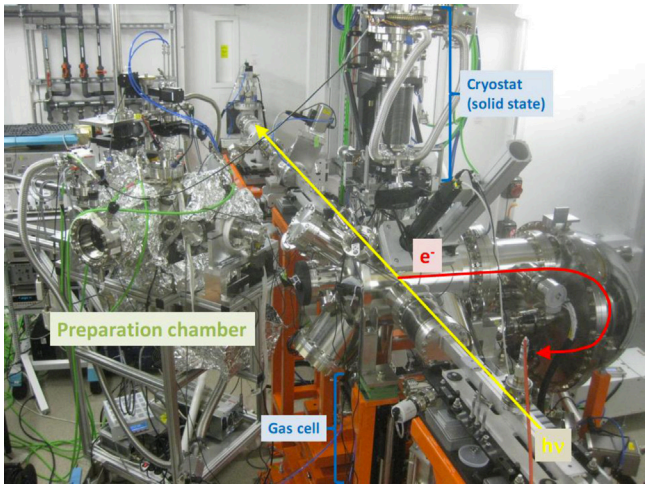

Figure 3.5: The HAXPES end-station of the GALAXIES beamline at SOLEIL [44]. The yellow arrow represents the incoming, linearly polarized radiation, whilst the red curved arrow shows the trajectory of the ejected electrons within the electron analyser.

in such case will be reduction in signal, necessitating longer acquisition times for a spectrum of desired statistics. The parameters are optimized to find a compromise between a resolution which allows the observation of the desired process and a relatively short acquisition time (∼12h). The pass energy of the EW4000 analyser can be in the range of 10 - 500 eV, with $E_p = 500$ eV being usually the pass energy chosen in order to record a sufficient number of electrons, for unambiguously identifying DCH pre-edge states. The total experimental resolution will be determined by the analyser conditions and the photon bandwidth. Assuming a narrow photon bandwidth, the electron analyser can detect electrons having a kinetic energy up to 10 keV, with a resolution of 35 meV [44]. In order to obtain higher count rates, the present work used mainly large pass energies (500 eV) and slits, resulting typically in an overall resolution of 1 eV.

The electrons exit the analyser and hit a micro-channel plate (MCP) detector, which amplifies the electron signal, by several orders of magnitude compared to the initial signal. The MCP is coupled to a charge-coupled device (CCD) camera, the latter allowing one to obtain a spatially resolved image of the photoelectron pattern. The HAXPES end-station is depicted in Figure 3.5, taken from Ref. [44].

3.4 Energy calibration

The energy calibration of the experimental data has been performed in two steps. First the kinetic energy scale of the electron spectrometer has to be established and that can be achieved by measuring the well-known argon LMM Auger spectrum, shown in Figure 3.6, and comparing the position of

the measured $L_3M_{2,3}M_{2,3}(^1S_0)$ peak with the literature value of 201.09 eV [47].

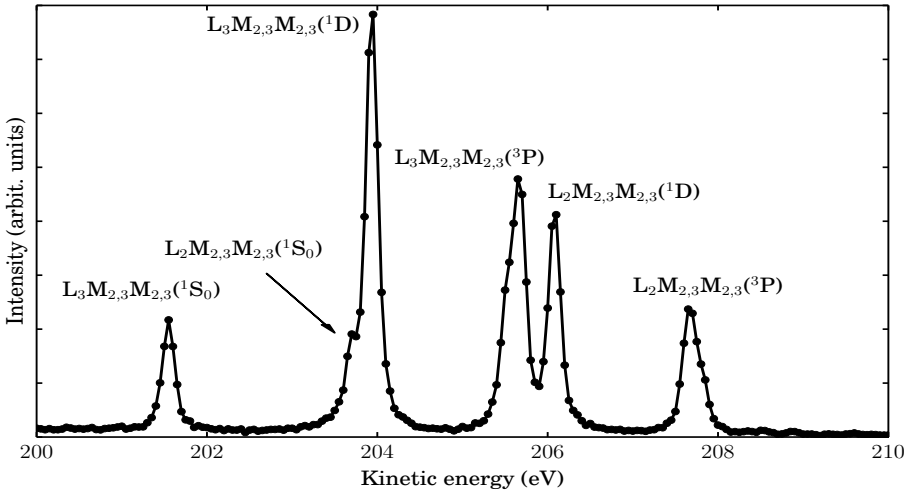

Figure 3.6: The LMM Auger spectrum of argon. The very first peak appearing at ∼201 eV kinetic energy can be used in order to perform a kinetic energy calibration of the acquired electron spectra.

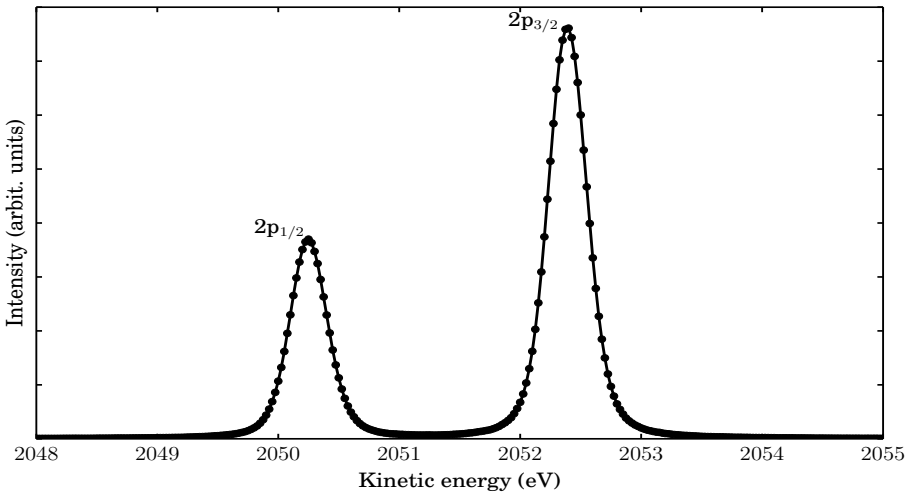

Figure 3.7: The argon 2p photoelectron lines measured at a photon energy $h\nu$ =2300 eV. The pass energy for this measurement was set to 200 eV.

After the kinetic energy scale has been established, the value of the photon energy can be calibrated by measuring the kinetic energies of well-known photoelectron lines. For the samples used within this thesis the lowest photon energy of the GALAXIES beamline (2300 eV) was usually sufficient in order to observe the processes we were interested in. For this photon energy, measuring the kinetic energy of the argon 2p photoelectron lines, as shown

in Figure 3.7 is enough to estimate deviations in the photon energy. This can be done by adding to the literature value of 248.63(4) eV [48] for the binding energy of the argon $2p_{3/2}^{-1}$ line, the measured kinetic energy of this transition, thus estimating an accurate value for the photon energy.

If a higher photon energy has been used the same procedure can be repeated using instead e.g. the argon 1s photoelectron line and its binding energy literature value of 3206.3(3) eV [49]. Generally, during the calibration, the experimental conditions (pass energy, width of slit) should be the same as the ones used for the data acquisition. As the signal from the Auger lines and the argon 2p lines is very strong, the undulator may need to be detuned in order to avoid saturation of the detector.

3.5 Time-of-flight coincidence spectroscopy

In this section we shall describe the main idea and the setup of time-of-flight (TOF) electron coincidence spectroscopy, using a magnetic bottle spectrometer of a type similar to that originally developed by J.H.D Eland [50]. In contrast to high-resolution spectroscopy, where the kinetic energy of an electron can be measured by its deflection within an electrostatic field, the idea in TOF spectroscopy is to obtain the kinetic energy of an electron by measuring the time it takes to move a known distance. From this, the velocity and subsequently the kinetic energy of the electron can be derived. For this purpose a magnetic bottle spectrometer, shown in Figure 3.8, can be used.

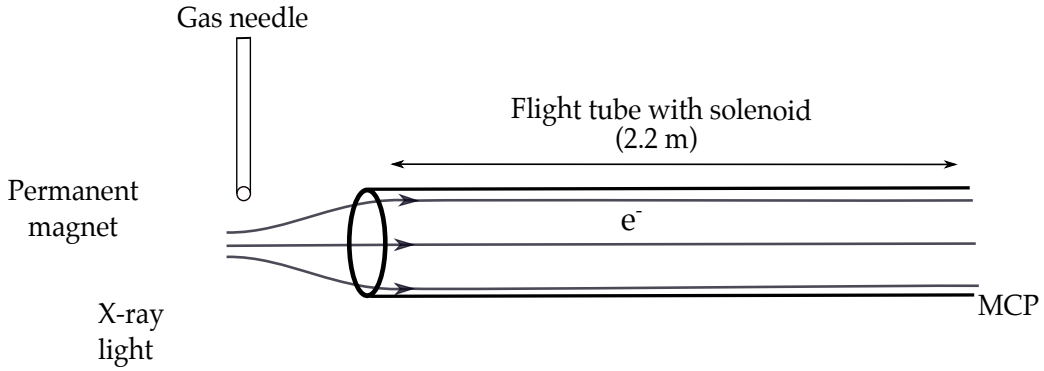

Figure 3.8: In a magnetic bottle spectrometer all the electrons are guided towards the detector, after they are collimated by the magnetic field of a strong (∼1T) permanent magnet and a weak (∼1mT) solenoid. By measuring the travel times of the electrons in the flight tube, one can estimate their velocity and subsequently their kinetic energies can be obtained.

In the setup shown in Figure 3.8, the region where the field from the permanent magnet, the gas needle and the incoming light intersect is referred to as the interaction region, which is where ionization of the sample takes place. The sample is let into the system via the gas needle and the ejected electrons are then captured by the magnetic field created by the strong permanent magnet and a weak solenoid wound around the flight tube, with the field lines'

shape resembling that of a bottle. This field, which functions as a magnetic mirror [51], can capture all the ejected electrons, independent of their ejection direction, thus essentially all the electrons can be collected and recorded. The electrons are guided to an MCP detector at the other end of the, in our setup, 2.2 m long flight tube. In order to protect the magnetic field in the flight tube from any external fields, the tube is shielded by μ-metal (not depicted in Figure 3.8).

A key aspect for performing TOF measurements is timing, since what is measured is the flight time of an electron until it is recorded by the detector. Thus, there must be a well defined start in the measurement. Though there are several timing schemes [52], the most straight forward one is to use a light detector and the ionizing light itself. A crucial factor here is the repetition rate between consequent light pulses. Due to the fact that we are interested in the outcome after the absorption of a single photon, if the time period between two pulses is shorter than the time it takes for the slower electrons to reach the detector, then the signal from two different ionization events may mix, as the fast electron from the second ionization event might reach the detector faster. Because of this, when performing TOF spectroscopy at synchrotron radiation facilities, like BESSY II in Berlin, it is important that the storage ring is operated in single-bunch mode. Even in this case, it is still possible to mix events coming from different ionizing pulses since the inter-pulse spacing is only $\sim$800 ns. For this reason, a mechanical chopper has been developed [53], which has been designed to reduce the repetition rate of the storage ring. The chopper is installed just before the experiment, in this way allowing the light to reach the interaction region after every tenth pass of the electron bunch for example. The reason that we want to record electrons coming from different ionization events separately is because in this way coincidence spectroscopy can be performed unambiguously and the correlations of several recorded electrons can be retrieved more easily. For the purposes of this thesis, DCH continuum and pre-edge states have been identified by simultaneously recording three electrons, emerging from the same ionization event (one photoelectron, two Auger electrons).

A final point before ending this brief description of the TOF coincidence spectroscopy technique is to describe the process of converting from a TOF scale to an energy scale. From classical mechanics we have:

$$E_{\mathrm{k}} = \frac{m_e v^2}{2} = \frac{m_e d^2}{2t^2} \qquad (v = d \cdot t), \tag{3.4}$$

with d being the length of the flight tube, t the electron time of flight, v the electron velocity and E_{k} the kinetic energy. Since the time delay between the occurrence of an event and its registration should be taken into account, as well as potential electrostatic fields in the interaction region, equation 3.4 can be re-written in the form:

$$E_{\mathrm{k}} = \frac{D^2}{(t - t_0)^2} + E_0, \tag{3.5}$$

where D is related to the length of the electron path, t_0 to the electronic delay time and E_0 to the potential electrostatic fields in the interaction region. All three parameters can be estimated as free fit parameters, by measuring the TOF spectra of species with well-known energies.

3.6 The complementarity of the two experimental techniques

From the descriptions of high-resolution electron spectroscopy using the HAXPES setup and the TOF electron coincidence spectroscopy, the complementarity of the two techniques might have started to become obvious, nonetheless it will be further emphasized in this short section. A study of DCH pre-edge states of CO_2 using both techniques can be found in Ref. [54].

Starting from TOF electron coincidence spectroscopy, we can see that collecting all electrons results in high count rates and allows the selection of a specific process, thus both DCH continuum and pre-edge states can be observed, along with the decay paths of such states, all in a single measurement. Moreover, TOF spectroscopy can give useful insight on the sharing of the excess energy by the ejected electrons. In contrast, the energy resolution offered by magnetic bottle spectrometers is usually $(\Delta E/E) \sim 1/50$ [52], which is less ideal for HAXPES experiments, where the ejected photoelectrons have very high kinetic energies.

The enhanced energy resolution offered by the HAXPES setup makes it suitable for the detection of DCH pre-edge states and allows for a detailed fit analysis of the acquired spectra, from which dynamical information can be obtained, e.g. the lifetime broadening [34] of DCH states or the slope of a potential energy curve [55]. Furthermore, high-resolution electron spectroscopy can be proven to be an indispensable tool for studying vibrational excitations of DCH states, as well as for measurements where the polarization of the incoming light can be varied allowing to obtain angular information, which is not so easily retrieved in TOF spectroscopy, using a magnetic bottle spectrometer. In this way, an experimental separation of the direct from the conjugate path can be achieved, when they are both present in a transition. However, the HAXPES technique runs into limitations if spectral features originating from different ionization processes overlap in energy, which would require a coincidence detection scheme to disentangle.

Chapter 4

Results

In this chapter, a detailed presentation of the results obtained within the framework of this thesis will be given. Most of the results concern the creation of DCH pre-edge states in molecules. The formation of DCH continuum states is also reported. Finally, a discussion about the observation of nuclear dynamics in water by Auger spectroscopy after the creation of several types of DCH states is given.

4.1 Rydberg states in HCl

In the first paper included in this thesis (Paper I), two different types of DCH pre-edge states in HCl have been observed, namely $1s^{-1}2p^{-1}(^{1,3}P)\sigma^*,n\ell$ and $1s^{-1}2s^{-1}(^{1,3}S)\sigma^*$, 4s. In this notation, the excited electron has occupied either the lowest unoccupied molecular orbital (LUMO) of HCl, which is an anti-bonding σ^* molecular orbital or an $n\ell$ atomic-like Rydberg state, with n, ℓ as defined in Chapter 2. Furthermore, double-shake-up transitions, of the form $1s^{-1}2p^{-1}V^{-1}n\ell\lambda n'\ell'\lambda'$, where the ionization of a core electron is accompanied by the simultaneous excitation of a core and a valence (V) electron, are also present in the recorded photoelectron spectrum, shown in Figure 4.1.

As in this case we have partially filled shells, spin-orbit coupling will give rise to singlet and triplet multiplicities, with the triplet being lower in energy, in agreement with what has been found for the same type of DCH states for argon [33]. The binding energy region from 3070 eV to 3100 eV corresponds to the $1s^{-1}2p^{-1}(^{1,3}P)\sigma^*,n\ell$ DCH region; it has been assigned based on a fit model and the results of *ab initio* quantum chemical calculations. The relative intensities in Figure 4.1 are given in units of 10^{-4} of the intensity of the Cl $1s^{-1}$ SCH peak. The region above 3130 eV corresponds to the formation of $1s^{-1}2s^{-1}(^{1,3}S)\sigma^*$,4s DCH states and the binding energy region in-between the two to the formation of double-shake-up states.

In the first binding energy region, two processes can take place. After single-photon absorption, either the 1s electron will be ionized, with a simultaneous excitation of the 2p electron to a np unoccupied orbital or the opposite, where a 2p ionization accompanied by a 1s$\rightarrow$ ns excitation will take place. As the 1s electrons significantly screen the 2p orbital, 1s ionization will result in a strong shake effect due to the change in the 2p radial distribution, thus np final states will appear as more intense peaks in Figure 4.1.

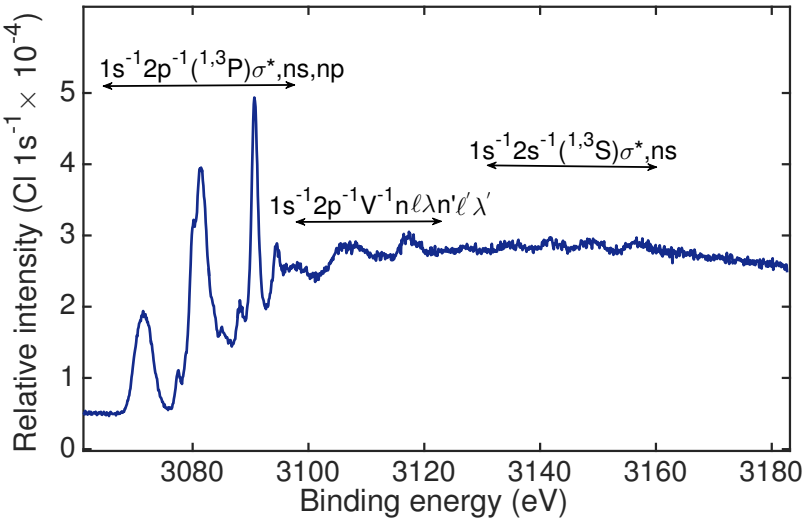

Figure 4.1: Photoelectron spectrum of HCl, recorded at a photon energy of 3900 eV, depicting the formation of $1s^{-1}2p^{-1}(^{1,3}P)\sigma^*,n\ell$ and $1s^{-1}2s^{-1}(^{1,3}S)\sigma^*$,4s DCH states, as well as the formation of $1s^{-1}2p^{-1}V^{-1}n\ell\lambda n'\ell'\lambda'$ double shake-up states.

In order to extract physical information like the lifetime and dissociative broadening for these specific DCH states, a fit model was implemented, where transitions to the LUMO have been fitted with a Gaussian function of ≈ 4.13 eV full width at half maximum (FWHM) in order to account for the projection of the ground-state vibrational wavefunction to the dissociative final state, through the Franck-Condon region as shown in Figure 2.5. Moreover, because of the triplet multiplicity, three different Gaussian functions have been used for the peak at $\approx$ 3072 eV. The Rydberg states have been fitted using a Lorentzian of $\approx$ 630 meV FWHM to account for the lifetime broadening. As the spacing between adjacent Rydberg states is proportional to n^{-3}, their density will be proportional to n^3, and will significantly increase close to the double-ionization threshold, resulting in the appearance of a background in the spectrum, which can be described by an arctan function (this background will be further discussed in Section 4.5) [56]. The inflection point of this arctan function is expected at the energy position of the first unresolved Rydberg state, which is in this case around 2 eV below threshold. For the $1s^{-1}2p^{-1}$ DCH region, four such functions have been used, as there will be four different DIPs there. Finally, convolution with a Gaussian of 585 meV was done in order to simulate the experimental resolution. The fit result, along with a detailed peak assignment, can be seen in Figure 4.2.

Subsequently, equation 2.1, which gives the energy levels of a hydrogenic atom has to be slightly modified, in order to give an estimate of how strongly an electron feels the nuclear charge. If the nuclear charge is perfectly screened for a specific electron by all the other electrons, it can be considered that this electron will simply feel a $+e$ nucleus, thus equation 2.1 can be applied. If the wavefunction of an electron can have a significant value close to the nucleus,

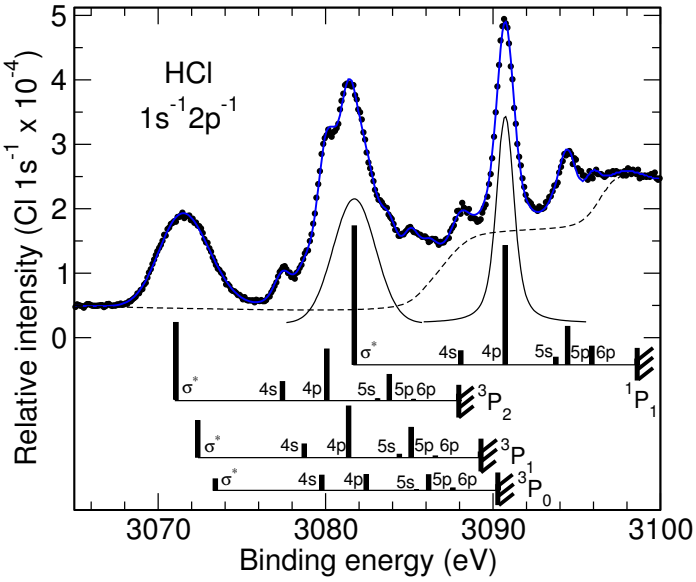

Figure 4.2: The blue line is a fit result for the $1s^{-1}2p^{-1}$ binding energy region of the spectrum. Transitions to the LUMO have been fitted using a Gaussian profile and the Rydberg states using a Lorentzian profile. The position of each transition, along with the corresponding DIP for each spin-orbit term, are shown with vertical bars. Finally, the dashed line represents the arctan background.

thus the electron can feel the nuclear charge, equation 2.1 can be modified as [57]:

$$E_n = -\frac{Z^2 \cdot \mathrm{Ry}}{(n-\delta_\ell)^2}, \tag{4.1}$$

where the quantity δ_ℓ is called the quantum defect [57]. As the energy position, E_n, has been extracted from the fit analysis for ns and np Rydberg electrons, the DIP and the quantum defects can be extrapolated, as free fitting parameters in the formula:

$$E_n = \mathrm{DIP} - \frac{Z^2 \cdot \mathrm{Ry}}{(n-\delta_\ell)^2}, \tag{4.2}$$

with $Z = 2$ to account for the double core vacancy. It was found that the quantum defect for ns electrons is $\delta_s = 1.76$ and for np electrons $\delta_p = 1.35$, while the obtained DIP for each spin-orbit term is given in Table 4.1.

Table 4.1: The extrapolated $1s^{-1}2p^{-1}$ DIP for each spin-orbit term, extrapolated from equation 4.2.

$1s^{-1}2p^{-1}$	$^3P_2$	$^3P_1$	$^3P_0$	$^1P_1$
DIP (eV)	3087.99	3089.29	3090.34	3098.64

4.2 DCH pre-edge structures of CH_3CN

Paper II reports on the formation of $K^{-2}V$ states in CH_3CN, which involve both the K shells of N and C atoms, as displayed in Figures 4.3 and 4.4 respectively, along with the results of *ab initio* quantum chemical calculations. The experimentally recorded photoelectron spectra are in very good agreement with the predictions obtained from the theoretical model described in detail in Refs. [13, 14], interpreting the observed spectral structures in terms of direct and conjugate transitions, as described at the end of Chapter 2. Also, as the molecule possesses two non-equivalent C atoms, initial and final state effects contributing to the chemical shift have been investigated and are discussed with the help of a Wagner plot.

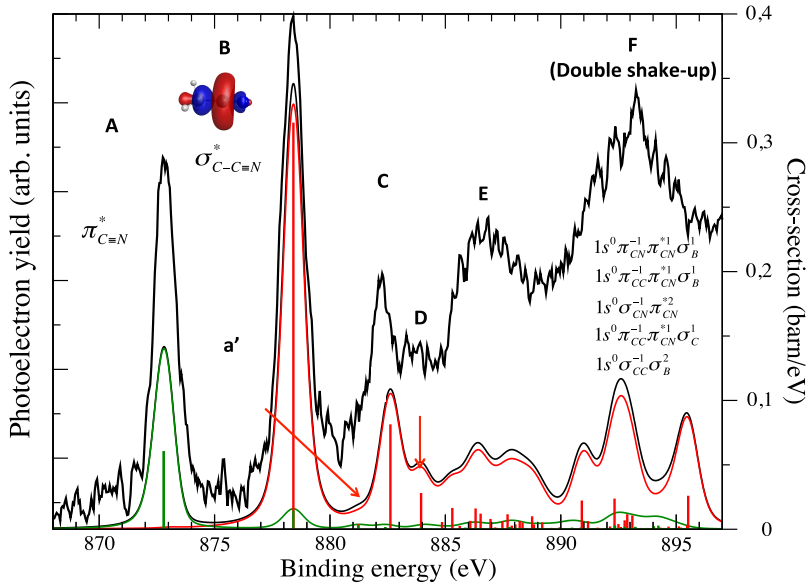

Figure 4.3: Photoelectron spectrum of CH_3CN recorded at a photon energy $h\nu = 2300$ eV, showing the formation of N $K^{-2}V$ DCH states (black line), along with the theoretical spectrum. The red (green) bars, in the theoretical spectrum, stand for the direct (conjugate) character of each transition. The notations σ_B and σ_C in the double shake-up region (peak F) correspond to transitions in the a_1 type orbitals of peaks B and C.

To begin with, it is mentioned that a K-shell excitation within the direct path will be characterized by an overlap integral of the form $\langle f|i\rangle$, which will be non-vanishing only if the final state orbital $|f\rangle$ and the initial state orbital $|i\rangle$ are of the same symmetry. Given that the molecule belongs to the C_{3v} point group, the possible final state orbitals can be a_1, a_2 and e, but as the symmetry of the initial 1s orbital is a_1, it should be the same for the final-state orbital. In contrast, the dipole transition within the conjugate path will be described by integrals of the form given in equation 2.6. The integral can be evaluated for

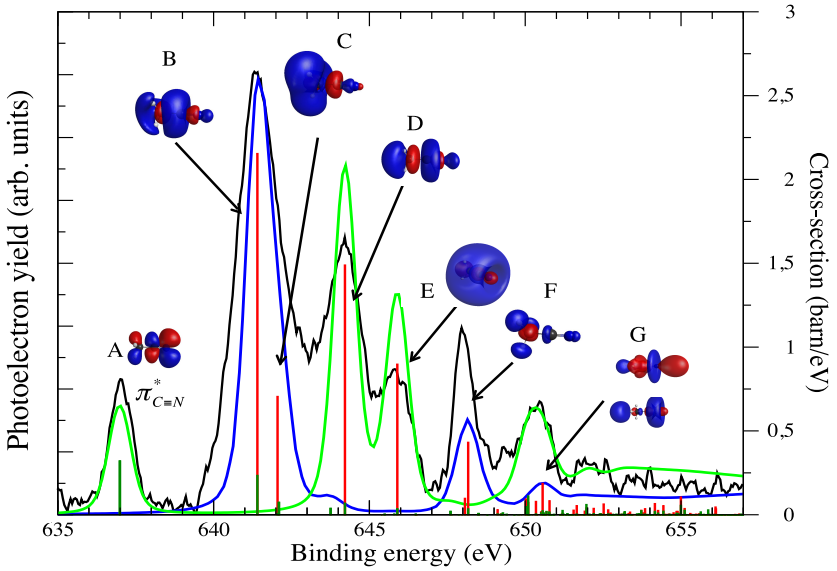

Figure 4.4: Photoelectron spectrum recorded at a photon energy of $h\nu = 2300$ eV, showing the formation of C $K^{-2}V$ DCH states of CH_3CN (black line), along with the theoretical spectrum. The red (dark green) bars, reflect as in the case of Fig. 4.3, the direct (conjugate) character of each transition. Transitions in blue (light green) in the theoretical spectrum show the formation of DCH pre-edge states involving the CH (CN) carbon atom.

each component of the dipole moment operator $\vec{D}$ separately and the character table of the C_{3v} point group can be used in order to identify which integrals are vanishing (meaning that the transition is forbidden) and which are non-vanishing. It can be proven that transitions of the form $\langle a_1 | \vec{D} | a_1 \rangle$ and $\langle e | \vec{D} | a_1 \rangle$ can take place, while transitions of the form $\langle a_2 | \vec{D} | a_1 \rangle$ are forbidden. In the photoelectron spectra of Figures 4.3 and 4.4, transitions reflecting the direct path are shown in red, while those reflecting the conjugate path are shown in green. It can be seen that there are transitions caused by both paths, with the direct channel being the dominant one.

Another point that should be addressed regarding the photoelectron spectra in Figures 4.3 and 4.4 is that while the observation of atomic-like Rydberg states similar to the case of HCl (Paper I) is expected, our theoretical results nevertheless indicate a non-negligible valence character of the final states reached, thus a definite assignment in terms of Rydberg states is not possible. This is why the symmetries within the given point group have been used to assign these peaks (Paper II).

4.2.1 Initial and final state effects

The purpose of this subsection is to apply the equations presented in Section 2.5 in order to estimate the chemical shift between the two C atoms in CH_3CN. Before moving forward, it should be pointed out, that as ss-DCH

exhibit large orbital relaxation effects, the relaxation-correlation energy given by $RC = R + C$ will be $RC \approx R$ for $R \gg C$.

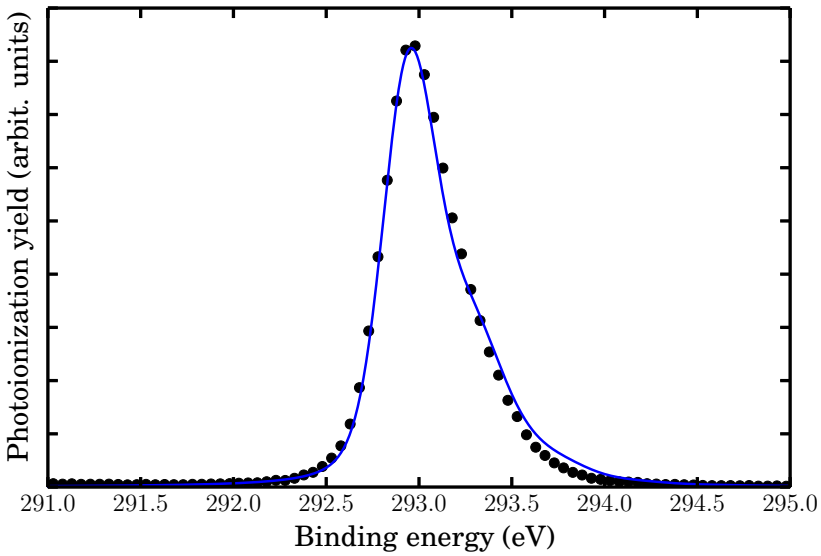

Figure 4.5: The C K^{-1} photoelectron spectrum of CH_3CN, recorded at a photon energy $h\nu$=2300 eV. The blue solid line through the experimental black data points is the convolution of the theoretical spectrum with a Gaussian of 270 meV FWHM accounting for the experimental resolution. The observed asymmetry is a manifestation of the vibrational progression taking place during core ionization.

Now equations 2.4 and 2.13, in combination with the measured and calculated ionization potentials, can be used to determine the contributions to the chemical shift between the two carbon atoms, namely the relative differences in orbital and relaxation energies. Furthermore, the validity of the results obtained from equations 2.15 and 2.17 can be tested by comparing them with the results obtained through quantum chemical calculations (Paper II). The IPs of C in CH_3CN have been measured, and are shown in black dots, along with the result of *ab initio* calculations, in Figure 4.5. The blue line in Figure 4.5 shows the convolution of the theoretical results, namely the energy positions and intensities of the vibrational levels, with the lifetime broadening and the experimental resolution. The IP values for the CN and CH carbon atoms using density-functional-theory (DFT) and including vibrational corrections are 292.874 eV and 292.879 eV respectively, in agreement with our experimental findings, calibrated according to the value of 292.98(7) eV given in Beach *et al.* [58]. In addition, a splitting of 0.54(15) eV was found in Ref. [58], while the results obtained here indicate a splitting of 5 meV for the two carbon atoms.

To build on these findings, the differences in the orbital energies and relaxation energies $\Delta\epsilon$ and ΔR respectively can be estimated, from the values of DIP and IP, calculated with different methods. The use of theoretical values for the ionization potentials can be justified from the very good agreement

between the experimental and theoretical results, demonstrating the high accuracy of the calculations. From equations 2.4 and 2.13 and the approximation $ERC(A^{-2}) = 2RC(A^{-1})$ we will have:

$$\left.\begin{aligned}(\mathrm{DIP}-\mathrm{IP})_{\mathrm{CH}} &= \mathrm{IP}_{\mathrm{CH}} - 2\cdot R(\mathrm{C}^{-1}_{\mathrm{CH}}) + RE(\mathrm{C}^{-2}_{\mathrm{CH}})\\ (\mathrm{DIP}-\mathrm{IP})_{\mathrm{CN}} &= \mathrm{IP}_{\mathrm{CN}} - 2\cdot R(\mathrm{C}^{-1}_{\mathrm{CN}}) + RE(\mathrm{C}^{-2}_{\mathrm{CN}})\end{aligned}\right\} \tag{4.3}$$

Subtracting by parts equations 4.3, defining $\Delta R = R(\mathrm{C}^{-1}_{\mathrm{CH}}) - R(\mathrm{C}^{-1}_{\mathrm{CN}})$ and keeping in mind that the Coulomb repulsion is independent of the environment and depends only on the specific atom, thus $RE(\mathrm{C}^{-2}_{\mathrm{CH}}) = RE(\mathrm{C}^{-2}_{\mathrm{CN}})$ we get for ΔR:

$$\Delta R = -\frac{(\mathrm{DIP}-\mathrm{IP})_{\mathrm{CH}} - (\mathrm{DIP}-\mathrm{IP})_{\mathrm{CN}} - (\mathrm{IP}_{\mathrm{CH}} - \mathrm{IP}_{\mathrm{CN}})}{2}. \tag{4.4}$$

With ΔR known, one can obtain the difference in orbital energies $\Delta\epsilon = \epsilon^{\mathrm{CH}} - \epsilon^{\mathrm{CN}}$, in a similar way as before:

$$\left.\begin{aligned}\mathrm{IP}_{\mathrm{CH}} &= -\epsilon^{\mathrm{CH}} - R(\mathrm{C}^{-1}_{\mathrm{CH}})\\ \mathrm{IP}_{\mathrm{CN}} &= -\epsilon^{\mathrm{CN}} - R(\mathrm{C}^{-1}_{\mathrm{CN}})\end{aligned}\right\} \tag{4.5}$$

and by subtracting by parts equations 4.5, we obtain:

$$\Delta\epsilon = -(\mathrm{IP}_{\mathrm{CH}} - \mathrm{IP}_{\mathrm{CN}}) - \Delta R. \tag{4.6}$$

The results obtained by applying equations 4.4 and 4.6 for the values of IP and DIP calculated with different quantum chemicals methods, like Hartree-Fock (HF) and DFT can be compared with the exact values if we use the results for ϵ and R obtained at the HF level of theory. Table 4.2 summarizes all the values.

Table 4.2: Calculated values of IP and DIP using different levels of theory, as well as the values of ϵ, $R(\mathrm{C}^{-1})$, $R(\mathrm{C}^{-2})$ and RE obtained at the HF level of theory. All values are given in eV.

	IP			DIP						
	HF	DFT	DFT(vib. cor.)	HF	DFT	DFT(vib. cor.)	ϵ	$R(\mathrm{C}^{-1})$	$R(\mathrm{C}^{-2})$	RE
CH	292.88	292.76	292.879	654.04	652.37	-	−307.11	14.23	56.44	96.26
CN	292.99	292.81	292.874	654.90	653.03	-	−306.87	13.88	55.10	96.26

From the values given in Table 4.2, the exact values for ΔR and $\Delta\epsilon$ are 0.35 eV and −0.24 eV respectively. Furthermore the ratio $R(\mathrm{C}^{-2})/R(\mathrm{C}^{-1}) \approx 3.97$ is very close to the value of 4 predicted by equation 2.17. Also the calculated values of RE are very close to those predicted by setting $Z = 6$ in equation 2.15. The estimated values of ΔR and $\Delta\epsilon$ from equations 4.4 and 4.6 are mentioned in Table 4.3.

Before discussing the physical meaning of these results, it is worth mentioning that in order to estimate the values of ΔR and $\Delta\epsilon$ from experimental values, one has to account for the vibrational progression of the molecule. As

Table 4.3: Estimated values for ΔR and $\Delta\epsilon$ from equations 4.4 and 4.6, for the values of IP and DIP obtained at different levels of theory. The exact values obtained at the HF level of theory are also included.

	ΔR (eV)	$\Delta\epsilon$ (eV)
HF	0.32	-0.21
DFT	0.28	-0.23
DFT(vib. cor.)	0.22-0.40	-0.22 to -0.40
Exact	0.35	-0.24

it was not possible within the framework of Paper II to either measure the DIP of the molecule or calculate it with the vibrational corrections included, the same values as the ones obtained from DFT without any vibrational corrections have been considered, with an error given by the difference of the DFT value of the IP including vibrational corrections minus the DFT uncorrected value, yielding $\pm$ 119 meV for CH and $\pm$ 64 meV for CN. Within these error bars, the values of ΔR and $\Delta\epsilon$ given in Table 4.3 have been obtained. From this we conclude that the measured values for DIP and IP can cause errors in the determination of $\Delta\epsilon$ and ΔR, which can be up to 0.2 eV due to the influence of the vibrational degrees of freedom. The results of Table 4.3 can be presented in the form of a Wagner plot, described in the following subsection.

4.2.2 Wagner plot representation

A way to present the results of Table 4.3 is in form of a Wagner plot, as shown in Figure 4.6, first suggested by T.D. Thomas [59], and subsequently used in the works of Ueda *et al.* [60] and Kryzhevoi *et al.* [61].

The main advantage of such a plot is that one needs to know only two experimentally measurable quantities, the IP and the DIP, in order to display in a relatively simple way the findings for $\Delta\epsilon$ and ΔR. More specifically, from equation 2.14 and by using once more the relation $ER(A^{-2}) = 2R(A^{-1})$, we get:

$$\mathrm{DIP} - \mathrm{IP} = \mathrm{IP} - 2R + RE. \tag{4.7}$$

As one has now on the vertical axis of a Wagner plot the difference DIP$-$IP and on the horizontal axis the value of IP, the slope α of a line connecting two points A, B in such a plot will be:

$$\alpha = \frac{(\mathrm{DIP}-\mathrm{IP})_\mathrm{B} - (\mathrm{DIP}-\mathrm{IP})_\mathrm{A}}{\mathrm{IP_B} - \mathrm{IP_A}} = \frac{(\mathrm{IP_B} - \mathrm{IP_A}) - 2(R_\mathrm{B} - R_\mathrm{A})}{(\mathrm{IP_B} - \mathrm{IP_A})} = 1 - \frac{2\Delta R}{\Delta\mathrm{IP}}, \tag{4.8}$$

with $\Delta\mathrm{IP} = \mathrm{IP_B} - \mathrm{IP_A}$ and $\Delta R = R_\mathrm{B} - R_\mathrm{A}$. Thus equation 4.8 can be written as:

$$-\frac{2\Delta R}{\Delta\mathrm{IP}} = \alpha - 1, \tag{4.9}$$

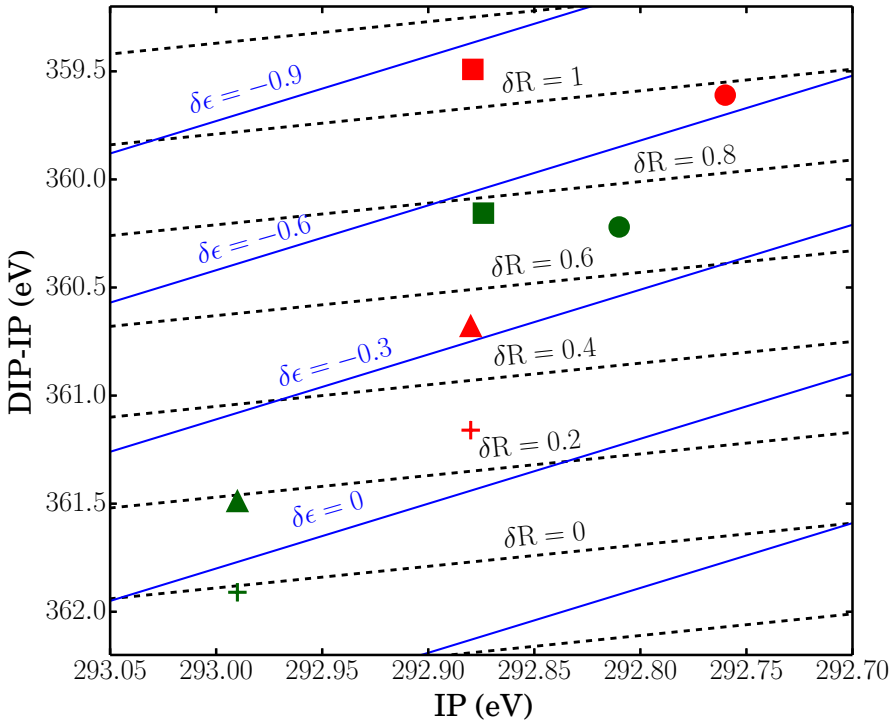

Figure 4.6: Along the blue solid lines the orbital energy remains constant and the same holds for the relaxation energy along the black dashed lines. All points in green refer to the C_{CN} atom, whilst all points in red refer to the C_{CH} atom. The different points in the plot indicated by squares, triangles, crosses and circles represent the values obtained with different methods (for more details see text).

from which it can be seen that along the lines with $\alpha = 1$ in Figure 4.6 (black dashed lines), $R = const$. Alternatively equation 4.8 can be written as:

$$-\frac{\Delta R}{\Delta \mathrm{IP}} = \frac{\alpha - 1}{2}, \tag{4.10}$$

which for $\alpha = 3$ gives $\Delta\mathrm{IP} = -\Delta R$ and because $\Delta\mathrm{IP} = -\Delta\epsilon - \Delta R$, from equation 2.4, we can see that along the lines having a slope equal to 3 in Figure 4.6 (blue solid lines) the orbital energy will have a constant value $\epsilon = const$.

The results given in Table 4.3 are presented in Figure 4.6. The crosses indicate the values obtained from HF calculations, whilst the squares and circles show the results of DFT calculations with and without vibrational corrections, respectively. For the former case, the values of DIP used were the ones corresponding to the lower limit, -119 meV for CH and -64 meV for CN. Furthermore, the triangles in Figure 4.6 correspond to the case where $R(A^{-2})$ is as in equation 2.17 and the DIP value has been calculated according to equation 2.11.

A final point that should be addressed here is the use of the symbols $\Delta\epsilon$ and ΔR. $\Delta\epsilon$ (ΔR) have been used to demonstrate that two core holes on a blue solid (black dashed) line have the same orbital energy ϵ (relaxation energy

R). These lines form a new, non-orthogonal coordinate system which provides the relative values for the orbital energy, $\delta\epsilon$, and the relaxation energy, δR. The absolute values are given by $\epsilon_{\mathrm{CH,CN}} = \epsilon_0 + \delta\epsilon_{\mathrm{CH,CN}}$ and $R_{\mathrm{CH,CN}} = R_0 + \delta R_{\mathrm{CH,CN}}$, where ϵ_0 and R_0 are two constant values. The subscripts CH and CN refer to the orbital or the relaxation energy of the corresponding carbon atom. By considering the differences in the orbital and relaxation energy between the two carbons, ($\Delta\epsilon$ and ΔR) one obtains $\Delta\epsilon = \delta\epsilon_{\mathrm{CH}} - \delta\epsilon_{\mathrm{CN}}$ and $\Delta R = \delta R_{\mathrm{CH}} - \delta R_{\mathrm{CN}}$.

Before moving on, the physical meaning of the obtained results shall be discussed. The higher negative orbital energy ϵ for the C_{CH} atom reflects a lower electron density on that atom, meaning that it is more difficult to remove an electron from it, though one would expect the opposite, thus a lower electron density in the region of the C_{CN} atom. This is due to the high electronegativity of nitrogen causing a lack of electrons in the vicinity of its neighbouring carbon atom. This latter effect is negated by the very short bond length between the two of them due to the triple bond character. Finally, the higher value of relaxation energy for the C_{CH} should be expected as the electron-donating hydrogen atoms can provide charge which screens the created core hole.

4.3 $K^{-2}V$ states of CS_2 and SF_6

An advantage of $K^{-2}V$ spectroscopy, is that it provides for molecules with sufficiently high symmetry, access to final-state orbitals, forbidden in conventional NEXAFS spectroscopy. This can be illustrated by considering the observation of $K^{-2}V$ states for the cases of the CS_2 and SF_6 molecules, reported in Paper III of the thesis. As the two molecules belong to different point groups, similar symmetry arguments as for the case of CH_3CN can be used, to identify the symmetry of the final-state orbitals reached.

The simpler case of the linear CS_2 molecule can be considered first, and more specifically the $K^{-2}V$ states involving the K shell of the C atom. As before, for the direct path, the $\langle f|i\rangle$ overlap integral will be non-vanishing only if the initial and final state orbitals are of the same symmetry. Within the $D_{\infty h}$ point group, to which the molecule belongs, the initial 1s orbital will be described by an a_{1g} orbital, thus direct transitions will have the general form $K^{-2}na_{1g}(n\sigma_g^*)$. This is a textbook example of the advantages of $K^{-2}V$ spectroscopy as g→g transitions are forbidden in conventional NEXAFS spectroscopy according to Laporte's selection rule for centro-symmetric molecules.

When considering the conjugate path, the angular momentum of the absorbed photon will result in a process which can be described as K(1s)→V(np (σ_u, π_u)), where the promoted K-shell electron will occupy a valence (V) orbital with a strong atomic p-orbital component. The latter can be manifested through the formation of σ or a π molecular orbital, having an ungerade parity, for the same reasons as before. The symmetries of the final states reached by conjugate transitions within the $D_{\infty h}$ point group will be $A_{1u}(\Sigma_u^+)$ and $E_{1u}(\Pi_u)$, thus the conjugate path will result in $K^{-2}na_{1u}(n\sigma_u^*)$ and $K^{-2}ne_{1u}(n\pi_u^*)$ final states.

The creation of a fully depleted K shell in one of the S atoms will lower the symmetry from $D_{\infty h}$ to $C_{\infty v}$, thus the inversion symmetry will be lifted. In this case we will have, for direct transitions, K(1s)→V(nsσ*), where a strong s-orbital character is expected. Similarly to the C case, conjugate transitions will have the general form K(1s)→V(np(σ*,π*)). In this case, both final state orbitals can be reached by NEXAFS spectroscopy as well.

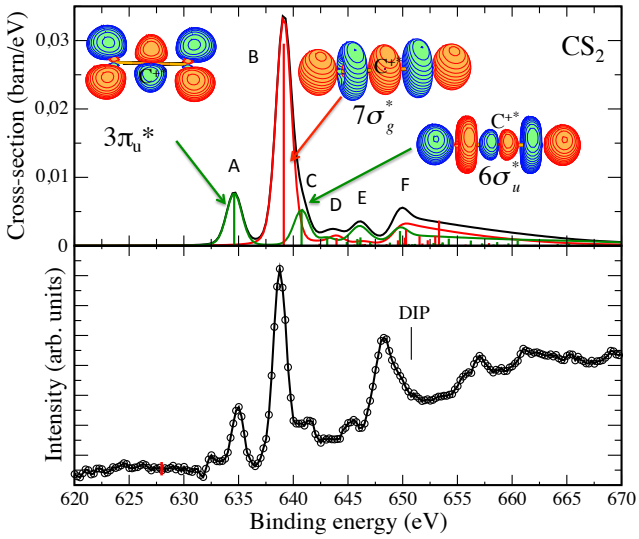

Figure 4.7: A theoretical (top) and an experimental (bottom) electron spectrum of CS_2, recorded at $h\nu$=2300 eV, showing the formation of $K^{-2}V$ states involving the K-edge of the C atom. The red (green) bars stand for the direct (conjugate) nature of each transition.

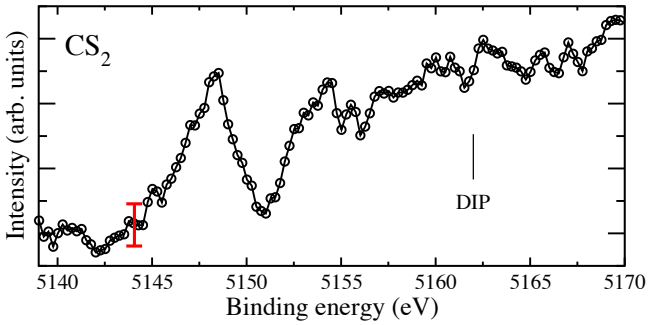

Figure 4.8: An experimental spectrum reflecting the formation of S $K^{-2}V$ states in CS_2, recorded at a photon energy of $h\nu$=5900 eV.

Continuing with the case of SF_6, one should consider the symmetries of the $K^{-2}V$ states involving the K shell of S and F separately, as it was found that the creation of a double vacancy in the K shell of the F atoms lowers the symmetry from O_h to C_{4v}. Starting from the $K^{-2}V$ states involving the K-shell of the S atom, direct transitions within the O_h point group will have the general form $K^{-2}na^*_{1g}$, leading to a final state orbital of g symmetry, non

reachable by NEXAFS spectroscopy, for the same reasons as before. For the conjugate path only integrals of the form $\langle t_{1u}| \vec{D} |a_{1g}\rangle$ will be non-vanishing, therefore conjugate transitions will have the general form $K^{-2}nt_{1u}^*$, as in the case of NEXAFS. For the creation of $K^{-2}V$ final states, involving the K-shell of

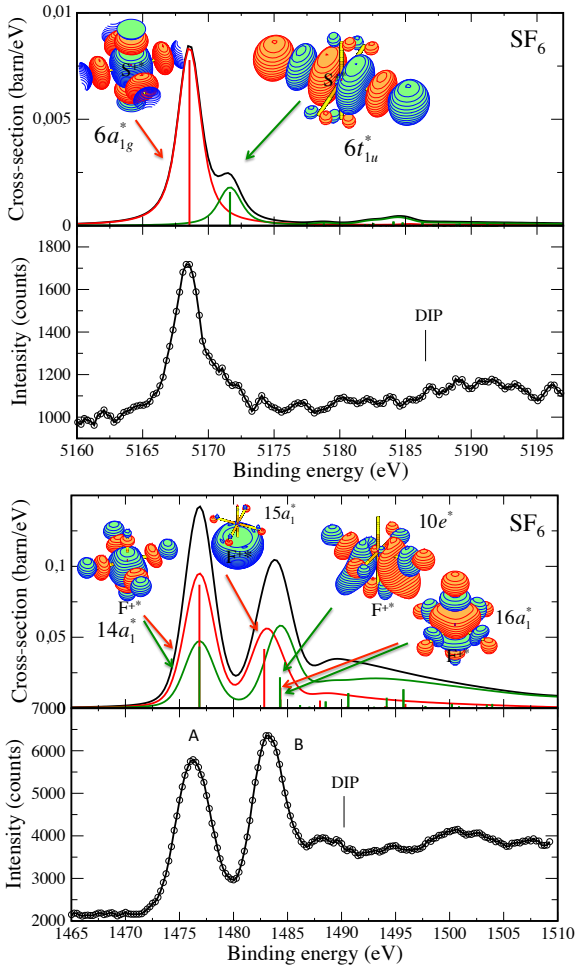

Figure 4.9: Experimental and theoretical spectra, showing the $K^{-2}V$ DCH in SF_6. On the top the S $K^{-2}V$ states have been recorded using a photon energy, $h\nu = 5900$ eV and on the bottom the F $K^{-2}V$ DCH states have been recorded at a photon energy $h\nu$=2300 eV. The red (green) bars indicate the direct (conjugate) character of each transition.

the F atoms, direct transitions can be shown leading to the occupation of an na_1^* valence unoccupied orbital upon the formation of a double K-vacancy, while two alternative final-state orbital symmetries exist for the conjugate path as both the $\langle a_1| \vec{D} |a_1\rangle$ and $\langle e| \vec{D} |a_1\rangle$ integrals are non-vanishing.

The experimental and theoretical spectra, showing the formation of C $K^{-2}V$ DCH states in CS_2 can be seen in Figure 4.7. The experimental photoelectron spectrum recorded at the K-edge of S is shown in Figure 4.8. The positions of the theoretically expected DIP are also indicated in both cases. Figure 4.9

displays the formation of $K^{-2}V$ DCH states involving the K-edges of both S and F of SF_6 along with the theoretical simulations of the spectra.

From the spectra shown in Figures 4.7 and 4.9, it can be seen that there is a very good agreement between the experimental results and the theoretical model described in Refs. [13, 14], especially for the energy position of each spectral feature. Some small intensity deviations can be seen by comparing the experimental and theoretical spectra. A very thorough theoretical simulation of these spectral features can become computationally expensive in terms of memory, thus in certain cases the above mentioned deviations have been observed.

4.4 Term values and shape-resonance shift under the formation of $K^{-2}V$ states

In this section a comparison of the peak positions corresponding to DCH pre-edge states in a photoelectron spectrum, with the peaks corresponding to the related transitions in the SCH case, recorded by means of inner-shell electron energy loss spectra (ISEELS) or NEXAFS spectroscopy shall be attempted. By considering the term value (TV) of each transition upon the formation of a double and a single core vacancy, it can be seen for the relative TVs that $TV_{DCH} \geq 2 \cdot TV_{SCH}$ (Papers II, III). Furthermore, the position of the transition which corresponds to what is referred to as shape resonance in the SCH case, was found to exhibit a significant shift since it was identified below the DIP (Papers II, III), contrary to the ISSELS and NEXAFS cases, where it was found to be well above threshold.

Concerning shape resonances, we remind ourselves that they are above-threshold, resonant processes [62]. It was suggested, more than thirty years ago, that the bond length of a molecule could be estimated by observing the recorded position of the shape resonance in a NEXAFS spectrum [63], an idea which was proved insufficient after thorough investigations [62, 64]. The final outcome was that although the position of a shape resonance should be sensitive to the bond length, a direct estimation of the bond length from only the position of the shape resonance can lead to ambiguous results.

A shape resonance is a one-electron process which can be viewed either as the trapping of the outgoing photoelectron from the molecular potential, from which it will tunnel, or as an unoccupied molecular orbital (MO) which can exist in the continuum [62, 64]. To begin with, in the ISEELS spectra of CH_3CN [65] the shape resonance (σ^*) had a TV of -16.9 eV with respect to nitrogen K^{-1} threshold and -15.5 eV, with respect to the C_{CN} K^{-1} threshold. In contrast, in Paper II it was found that the TV of $K_N^{-2}\sigma^*_{CCN}(a_1)$ (peak B in Figure 4.3) was ≈ 9.0 eV, with the K_N^{-2} threshold at 886.61 eV binding energy ,while the TV of the $K_{C_{CN}}^{-2}\sigma^*_{CCN}(a_1)$ (peak D in Figure 4.4) was ≈ 8.53 eV, with the $K_{C_{CN}}^{-2}$ threshold at 653.03 eV binding energy. An interesting case is presented in Paper III for the case of CS_2, where the $K_C^{-2}(6\sigma_u^*)$ transition has

been observed ≈ 10.0 eV below the K_C^{-2} DIP, nevertheless no $K^{-1}(6\sigma_u^*)$ transitions has been observed in the ISEELS measurements of Wight and Brion [66].

Other interesting examples are the cases of N_2 and CO_2 studied by Carniato *et al.* [14, 54]. In the first case the $K^{-2}\sigma^*$ transition was observed at ≈ 893.5 eV with the K^{-2} DIP at ≈ 902.5 eV, thus a TV of ≈ 9.0 eV was estimated. For the same molecule, the $K^{-1}\sigma^*$ transitions was found at ≈ 416.0 eV in the recorded ISEELS spectrum of Hitchcock *et al.* [67] and at ≈ 417.5 eV in the theoretical NEXAFS spectrum simulated by Carniato *et al.* [68]. As the K^{-1} IP has been found at 409.9 eV [67] a TV of ≈ -8.0 eV is estimated for this transition, thus a shift of ≈ 17 eV seems to be the case under the double K vacancy. For the case of CO_2 the $K_C^{-1}\sigma_u^*$ transition has been recorded at 313.8 eV by means of NEXAFS spectroscopy in the work of Sham *et al.* [69], with the threshold being at 297.5 eV [70], thus a TV of ≈ -16.0 eV has been found. The $K_C^{-2}\sigma_u^*$ of CO_2 has been found at ≈ 657.0 eV binding energy, with the K_C^{-2} threshold at 666 eV binding energy [54], thus for the DCH case the TV is $\approx$ 9.0 eV, suggesting a TV-shift of ≈ 25.0 eV for the fully depleted K shell.

From all these values a correlation between the position of what could be called a shape resonance for the DCH case and the bond length of the molecule becomes apparent, as upon the creation of a $K^{-2}V$ DCH state, two effects competing with each other take place. On one hand the hollow K shell will lead to the contraction of the orbitals towards the atom that possesses the two K-vacancies, as the electrons occupying them will now feel a higher nuclear charge. On the other hand, the excited electron occupies an anti-bonding MO which in turn will cause an elongation of the bond. The below-threshold observation of the shape resonance is in line with the MO orbital picture of the process and the orbital contraction mentioned above, rather than the back-scattering picture of the ejected electron between the parent and a neighbouring atom suggested in Ref. [63].

Table 4.4: A comparison of the TVs for different transitions in different molecules, under the formation of a single and a double K-vacancy.

	TV(eV)			
CH_3CN	$K^{-1}\pi^*$	$K^{-1}\sigma^*$	$K^{-2}\pi^*$	$K^{-2}\sigma^*$
N K-edge	5.7	-16.9	15.0	9.0
C K-edge	5.5	-15.5	16.03	8.53
CS_2	$K_C^{-1}3\pi_u^*$	$K_C^{-1}6\sigma_u^*$	$K_C^{-2}3\pi_u^*$	$K_C^{-2}6\sigma_u^*$
	7.0	-	16.09	10.0
N_2	$K^{-1}\sigma^*$		$K^{-2}\sigma^*$	
	-8.0		9.0	
CO_2	$K_C^{-1}\sigma_u^*$		$K_C^{-2}\sigma_u^*$	
	-16.0		9.0	

Finally, as was mentioned at the beginning of this section, increased TV are characteristic of $K^{-2}V$ spectroscopy. Beyond the σ^* transitions discussed in detail above, it was found for the case of CH_3CN (Paper II) that the TV of the $K_N^{-2}\pi^*_{CN}(e)$ transition was $\approx$ 15.0 eV, while the TV of the corresponding $K_N^{-1}\pi^*_{CN}$ transition in Ref. [65] was estimated to be 5.7 eV. Accordingly the TV of the $K^{-2}_{C_{CN}}\pi^*_{CN}(e)$ transition was estimated to be 16.03 eV, with the TV of $K^{-1}_{C_{CN}}\pi^*_{CN}$ transition at 5.5 eV [65]. Similarly, for the case of CS_2 (Paper III) the TV of the $K^{-2}(3\pi_u^*)$ transition was estimated to be 16.09 eV, with the TV of the corresponding $K^{-1}(3\pi_u^*)$ transition, recorded by means of ISEELS spectroscopy, estimated to be 7.0 eV [66]. All the above menioned values are summarized in Table 4.4.

4.5 Background in the experimental spectra

Earlier it was mentioned that in order to reproduce the $1s^{-1}2p^{-1}\sigma^*, n\ell$ DCH region in HCl (Paper I), we had to account for a background in the recorded spectrum, which can be described by an arctan function (one for each fine-structure term for both spin multiplicities). The same was found for the iso-electronic case of argon in Ref. [33]. A reason for the appearance of this background was given, which took into account the density of Rydberg states close to the double-ionization threshold.

From the recorded photoelectron spectra of CH_3CN (Paper II), in Figures 4.3 and 4.4 one can see that a background in the spectrum showing the $K^{-2}V$ states in the N K-edge (Figure 4.3), resembling an arctan function is visible, while no such background can be recognized for the spectrum recorded on the carbon sites (Figure 4.4). This observation is probably in line with the aforementioned argument about the nature of this background. Since CH_3CN possesses two carbon atoms, the formation of molecular orbitals between them should be favoured due to the energy pairing of the related atomic orbitals, in this way suppressing the atomic-like Rydberg states. Although from our calculations no atomic-like Rydberg states were found even for the case of N, we expect a significant Rydberg character in the final states that are reached through the transitions involving the K-shell of nitrogen, which in turn might manifest through the appearance of a background.

In contrast, the experimental findings for CS_2 and SF_6 (Paper III) further complicate things. For the case of CS_2, according to the previous argumentation, a background is expected for the S $K^{-2}V$ states as can be seen from Figure 4.8. For SF_6, no background should appear in the experimental spectrum showing the formation of F $K^{-2}V$ states and vice versa for the formation of DCH pre-edge states involving the K shell of the S atom. However, from Figure 4.9 it can be seen that exactly the opposite was observed, where the appearance of a background has been recorded for the F case.

Additional factors which could contribute to the formation of such a background might be molecular geometry (whether or not the atom under consideration has a terminal position in the molecule), as well as the fact that for all

of the cases mentioned in this thesis, the photon energy used to trigger the formation of the DCH pre-edge states was well above the associated DIPs. That means that double photo-ionization (the simultaneous ejection of two photoelectrons, that share the excess energy arbitrarily) was present while recording the pre-edge spectra. That could account for an increase of the recorded signal above the DIP, reflected in the formation of the background.

Beyond the above mentioned factors, the peak to background ratio can also be considered. In Paper II, according to our simulations the intensity of the main peaks appearing in the electron spectrum of N (Figure 4.3) is at ≈ 0.35 barn/eV, whilst for the C atoms (Figure 4.4) the intensity is at ≈ 2.5 barn/eV. For both cases though the experimental backgrounds appear at $\approx$ 0.2 barn/eV, suggesting that in the case of the N atom the background is discernible as the related spectral features are not as intense as in the C case. Nevertheless, considering again the case of SF_6 in Paper III, one can see that the intensity of the main line for the case of S $K^{-2}V$ states is at ≈ 0.0075 barn/eV (top panel of Figure 4.9), while from our experimental data the rescaled background appears at 0.002 barn/eV. On the bottom panel of Figure 4.9 it can be seen that the main lines concerning the formation of $K^{-2}V$ DCH states involving the F K-edge have an intensity of ≈ 0.15 barn/eV. By rescaling the experimental spectrum the background appears at ≈ 0.05 barn/eV. The peak to background ratio is 3.75 for the S and 3.0 for the F case, thus the two ratios are very close together, still the background becomes significant only in the latter case.

In summary, the nature of this background has not been fully understood yet, as the reasons leading to its formation are still unclear and should be further investigated, both experimentally and theoretically.

4.6 Nuclear dynamics upon the creation of a DCH state: The case of H_2O

Nuclear dynamics of singly/doubly core-ionized molecules, specifically the response of the molecular geometry within the lifetime of the core hole(s), is a topic that has been extensively discussed in the literature [71, 72, 73]. Nuclear dynamics can become particularly interesting when electron delocalization occurs, as it may lead to ambiguous experimental observations [74]. DCH spectroscopy has been suggested as a solution to this problem, as the very short lifetime of the highly excited DCH states will not allow for enhanced nuclear dynamics [75], though the strongly dissociative PES of DCH states have been shown to exhibit significant nuclear dynamics [76], resulting even in ultra-fast dissociation of the molecule [77, 78].

Nuclear dynamics in H_2O, upon the creation of a double K-shell vacancy on the O atom has been observed and discussed in Paper IV. More specifically the tail appearing in the high kinetic energy region ($\geq$500 eV) of the KLL Auger spectrum, shown in Figure 4.10, where the hyper-satellite Auger structures are expected (the Auger lines due to the decay of different types of DCH states) has been shown to be a clear finger-print of nuclear dynamics.

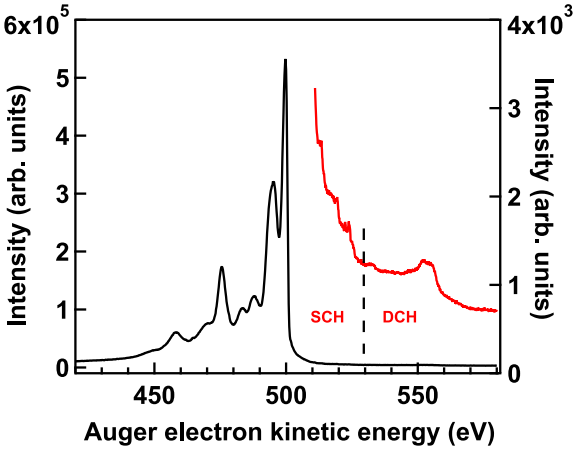

Figure 4.10: The KLL Auger spectrum of H_2O. The structures appearing at kinetic energies higher than 500 eV correspond to the Auger decay of different types of DCH states involving the K-shell of the O atom.

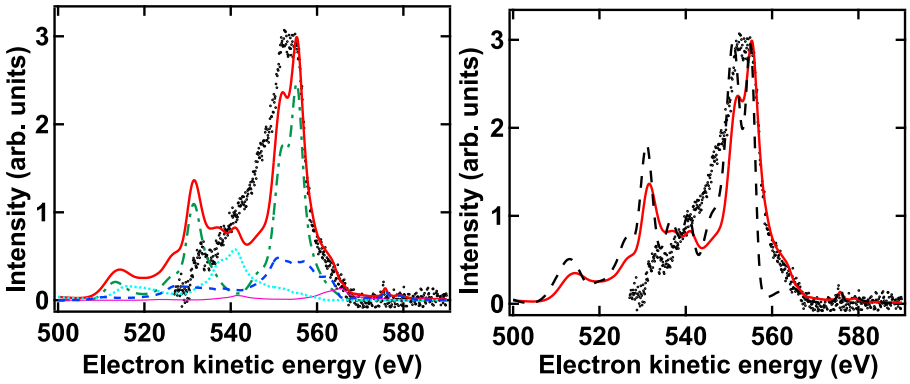

Figure 4.11: Left: The hyper-satellite Auger spectrum of H_2O (black dots), recorded at a photon energy $h\nu = 2300$ eV. The red solid line stands for the calculated Auger spectrum, taking nuclear dynamics into account. For its calculation the decay of several types of DCH states was taken into account and shown here. The K^{-2} contribution is in dashed-green, the $K^{-2}V$ in magenta, the $K^{-2}L^{-1}$ in dotted cyan and the $K^{-2}L^{-1}V$ in dashed-blue. Right: A comparison of the theoretical Auger spectrum, when nuclear dynamics has been taken into account (red) and when it has been neglected (dashed-black), with the experimentally recorded spectrum (black dots).

The recorded hyper-satellite Auger spectrum has been reproduced by a theoretical model taking into account the contributions of nine different DCH states, namely the K^{-2}, $K^{-2}4a_1$, $K^{-2}2b_2$, $K^{-2}3a_1^{-1}4a_1$, $K^{-2}2a_1^{-1}4a_1$, $K^{-2}1b_2^{-1}2b_2$, $K^{-2}3a_1^{-1}$, $K^{-2}2a_1^{-1}$, $K^{-2}2b_2^{-1}$ as shown in Figure 4.11. The contribution (relative weight) of each DCH state to the spectrum was the same as the one identified for the iso-electronic case of Ne [79]. The major contribution in the spectrum was found to be the one of the K^{-2} DCH states.

The *ab initio* calculations performed within the framework of Paper IV suggest that the formation of a K^{-2} DCH will lead to a subsequent symmetric dissociation of the molecule. The elongation of the OH bonds will be reflected in the hyper-satellite Auger spectrum, by shifting the dominant $1b_1^{-2}$ structure at $\approx$ 555 eV kinetic energy, towards higher kinetic energies, as illustrated in Figure 4.12. The reason for that shift can be found in the dissociative nature of

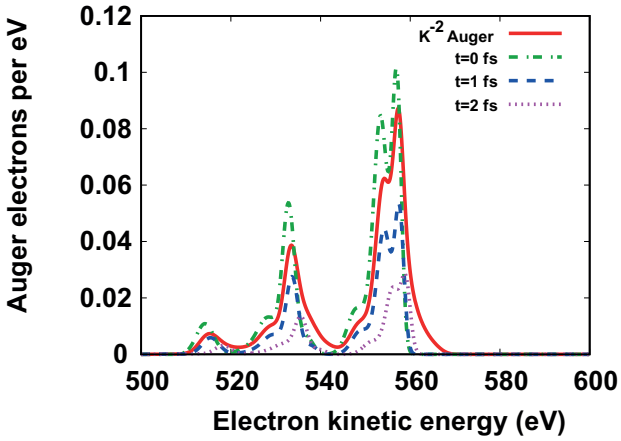

Figure 4.12: Time evolution of the hyper-satellite Auger spectrum of water. The shift of the main peak at $\approx$ 555 eV towards higher kinetic energies is a finger-print of nuclear dynamics (for more details see text).

the K^{-2} final state, leading to the elongation of the OH bonds with time and to the subsequent dissociation of the molecule. In turn that will change the positions of the valence orbitals and the latter will be reflected in the different kinetic energies that the Auger electrons will have.

4.7 The influence of the PEC slope in the broadening of the experimental peaks

As briefly mentioned in Section 2.4, the broadening of an experimental peak corresponding to an electronic transition from an initial bound state to a final dissociative state will strongly depend on the slope of the PEC. Let us now discuss this aspect in more detail for the case of a diatomic molecule. The nuclear part of the wavefunction of a dissociative electronic state will have the form shown in Fig. 4.13. These wavefunctions can be described by an oscillating function having a significant amplitude close to the potential energy curve and decaying exponentially as one moves away from it.

The Condon reflection approximation [29] states that instead of using this complicated mathematical form in order to account for the intensity profile of the peak, according to the Franck-Condon factors 2.10, one can simply replace each eigenfunction of the nuclear motion of the dissociative state by a δ function at the turning point. Then, because of $\int \delta(x-\alpha)f(x)\mathrm{d}x = f(\alpha)$, the

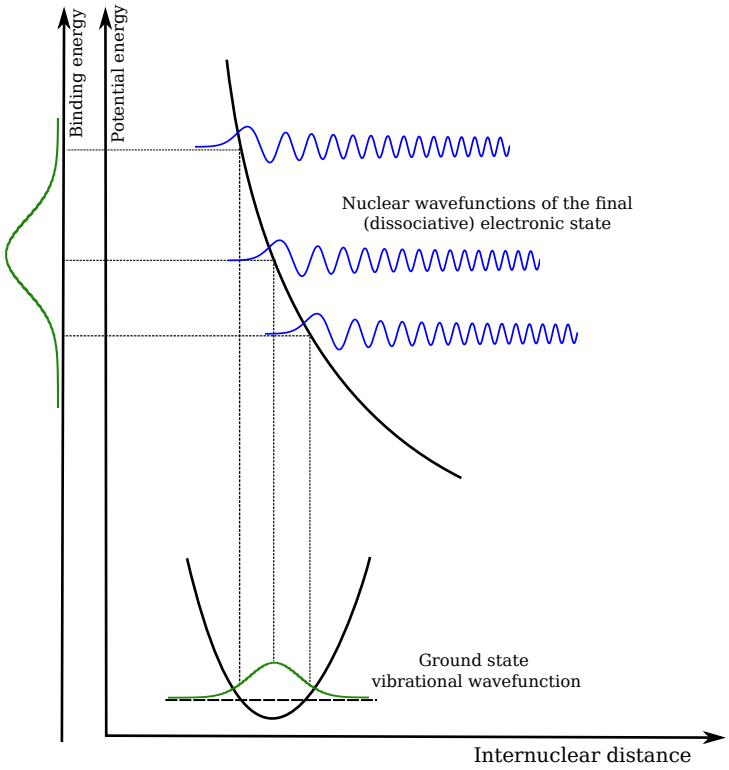

Figure 4.13: According to the Condon reflection approximation, the eigenfunctions of the nuclear motion at each "vibrational" level of the dissociative electronic state, can be approximated by a delta function at the classical turning point. In this way the intensity profile of the experimental peak can be obtained by reflecting each point of the squared ground vibrational wavefunction through the dissociative PEC (for more details see text). In this figure we have considered a harmonic oscillator potential for the PEC of the ground electronic state.

evaluation of the integrals 2.10 will result in the squared value of the vibrational ground state wavefunction at the corresponding internuclear distance, thus $\phi^2_{\text{vib}}(R)$, which according to Ref. [55] will be proportional to:

$$\phi^2_{\text{vib}}(R) \propto e^{-\alpha^2(R-R_e)^2}, \tag{4.11}$$

R being the internuclear distance, R_e the equilibrium bond length and α^2 in case of a diatomic molecule given by:

$$\alpha^2 = \frac{\mu\omega}{\hbar}, \tag{4.12}$$

μ being the reduced mass of the molecule and ω the vibrational frequency. Following Ref. [55], the line shape of the dissociative electronic state can be replaced by a straight line, making the intensity profile of the experimental

peak proportional to:

$$I(E) \propto \frac{1}{\sqrt{\pi}\sigma} e^{-\left(\frac{E-E_0}{\sigma}\right)^2}, \tag{4.13}$$

E_0 being the peak position and σ the width of the peak. By comparing the exponentials in the proportionality relations 4.11 and 4.13, the influence of the PEC slope S on the width of the peak becomes apparent:

$$S = \frac{E - E_0}{R - R_e} = \alpha\sigma. \tag{4.14}$$

The validity of equation 4.14 has been tested in Paper I of this thesis. As discussed in Section 4.1, the peaks corresponding to $1s^{-1}2p^{-1}\sigma^*$ transitions have been fitted with a Gaussian having a FWHM of 4.13 eV. The reduced mass of HCl is $\mu = 1.627 \times 10^{-27}$ kg and its vibrational frequency is $\omega = 8.66 \times 10^{13}$ Hz. From equations 4.12 and 4.14 we get a value for the slope, $S_{exp} = -15.1(1.3)$ eV·Å^{-1}, with the theoretically predicted value being $S_{th} = -12.9$ eV·Å^{-1}. We note that these values are in very good agreement with the theoretical value of $S_{th} = -14.5$ eV·Å^{-1}, calculated in Ref. [77] for the $2p^{-2}\sigma^*$ transitions in HCl.

4.8 Observation of DCH states by means of TOF coincidence spectroscopy

Complementary results reporting on the observation of K^{-2} and $K^{-2}V$ DCH states in C_4H_{10}, by means of TOF multi-electron coincidence spectroscopy were obtained (Paper V). This experimental work was performed at the BESSY II synchrotron radiation facility. The spectrometer setup shown in Fig. 3.8 was used and three electrons were recorded in coincidence. In contrast to single electron spectroscopy, where different $K^{-2}V$ DCH states are detected based on the kinetic energy of the ejected photoelectron, in coincidence spectroscopy the kinetic energies of the Auger electrons ejected due to the decay of such states can be used in order to locate the desired process.

To go into more detail, the formation and decay of a $K^{-2}V$ DCH can be described by the following scheme:

$$\begin{aligned} C_4H_{10} + h\nu &\rightarrow C_4H_{10}^{+} + e_{ph} \\ &\rightarrow C_4H_{10}^{2+} + e_{Auger1} \\ &\rightarrow C_4H_{10}^{3+} + e_{Auger2}, \end{aligned} \tag{4.15}$$

where e_{ph} denotes the ejected photoelectron and e_{Auger1} and e_{Auger2} the two Auger electrons emitted at each step of the decay of the double core-vacancy. A similar scheme as the one shown above can be used in order to describe the formation and decay of a K^{-2} DCH state, but this time we will have the

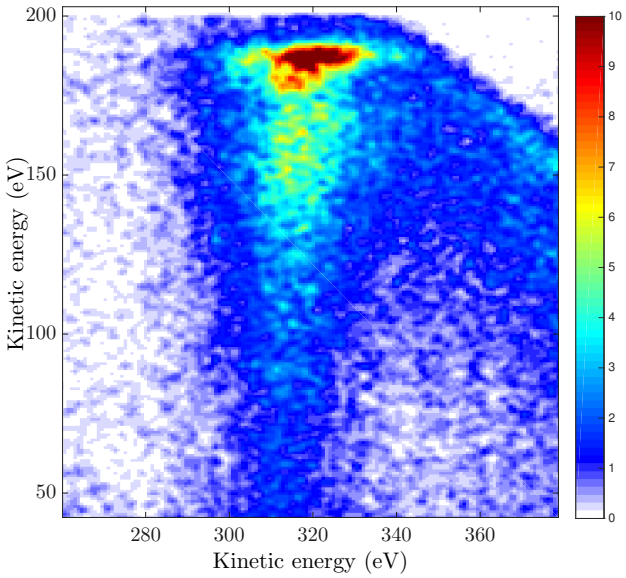

Figure 4.14: Coincidence map showing the formation of a $K^{-2}V$ DCH state in C_4H_{10} as an island at $\approx$ (320 eV, 180 eV). The kinetic energies of two out of the three recorded electrons are shown, when the kinetic energy of the third is in the range 200-260 eV, which corresponds to the kinetic energy of e_{Auger2}. The photon energy used was $h\nu = 821$ eV. For more details see text.

ejection of two photoelectrons:

$$\begin{aligned} C_4H_{10} + h\nu &\rightarrow C_4H_{10}^{2+} + e_{\text{ph1}} + e_{\text{ph2}} \\ &\rightarrow C_4H_{10}^{3+}/C_4H_{10}^{4+} + e_{\text{Auger1}} + e_{\text{Auger2}} \end{aligned} \tag{4.16}$$

Both processes 4.15 and 4.16 can be seen in Fig. 4.14, where the kinetic energy of two out of the three recorded electrons is displayed, with the kinetic energy of the third electron being in the range between 200-260 eV. This is the kinetic energy range of e_{Auger2}, as it was found for the related case of the C_2H_{2n}, $(n = 1, 2, 3)$ series studied in Ref. [32].

By looking at Fig. 4.14, one can see an island at (x, y)=(320 eV, 180 eV), corresponding to the formation of a $K^{-2}V$ DCH state. Moreover, the stripe at (x = 320 eV, y< 180 eV) is due to the higher unoccupied orbitals that the core-excited electron reaches, up to the K^{-2} limit, in agreement with what has been observed in [32]. From Fig. 4.14, we also see that the kinetic energy along the x-axis remains constant, while the kinetic energy along the y-axis decreases, suggesting that the x-axis reflects the first emitted Auger electron e_{Auger1}, and the y-axis the ejected photoelectron. The photoelectron spectra reflecting the $K^{-2}V$ and K^{-2} DCH states of C_4H_{10} can be seen in Fig. 4.15 and Fig. 4.16, respectively.

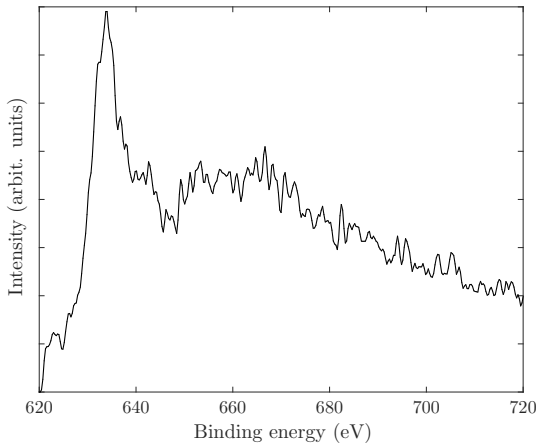

Figure 4.15: Photoelectron spectrum showing the formation of $K^{-2}V$ double-core-hole states in C_4H_{10}, measured at a photon energy $h\nu = 821$ eV.

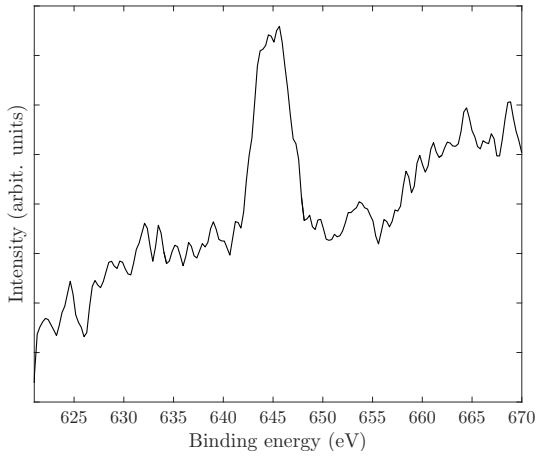

Figure 4.16: Photoelectron spectrum showing the double-core-hole continuum state in C_4H_{10} at ≈645.5 eV, measured at a photon energy $h\nu = 821$ eV.

Table 4.5: The experimentally measured and theoretically calculated energy positions of different DCH states in C_4H_{10}.

	Exp. (eV)	Theory (eV)
$K_1^{-2}V$	635	638
$K_2^{-2}V$	635	638
K_1^{-2}	645.5	648.29
K_2^{-2}	645.5	648.38

The position of the $K^{-2}V$ DCH state was found at ≈ 635 eV, while the K^{-2} threshold was measured at ≈ 645.5 eV. These values are in good agreement with the results obtained from *ab initio* calculations. The experimental

and theoretical results are summarized in Table 4.5. We note that the K_1 notation refers to the terminal C atom, and the K_2 to the neighbouring C atom of C_4H_{10}. Due to the symmetry of the molecule, the same theoretical results were obtained for the two remaining C atoms of the molecule, thus they have been omitted.

Chapter 5

Conclusions and outlook

The field of DCH spectroscopy is currently attracting a lot of scientific interest, and several research groups around the world are performing experiments focusing on the observation of DCH states using either SR or the radiation produced by an FEL. This thesis focused on the experimental observation of DCH states in molecules using SR.

The identification of atomic-like Rydberg states on the creation of a double core vacancy, the separation of initial and final state effects upon core-ionization, and their contributions to the chemical shift, as well as the different final-state symmetries of $K^{-2}V$ states and the fingerprints of nuclear motion in the decay patterns of DCH states were demonstrated in the thesis. In all these works, the formation of the double vacancy involved only one atom in the molecule. In addition, the increased TV of the observed spectral features, due to the strong attractive field of the double core-vacancy were discussed, and were found to have a value more than two times greater than the corresponding value in the SCH case. This aspect of $K^{-2}V$ spectroscopy can be used for a quick assessment of the recorded spectra when experimental work is performed.

Furthermore, the appearance of a pronounced background in the experimental spectra, which can be mathematically described by an arctan function was reported. The actual nature of this background has yet to be understood. Finally, the complementarity of HAXPES and TOF coincidence spectroscopy was demonstrated. Additional results were obtained using the latter technique, where both $K^{-2}V$ and K^{-2} DCH states were recorded.

Experimental findings on the creation of ts-DCH pre-edge states were also obtained, and while not covered by this thesis are the subject of current, ongoing analysis. Nevertheless, the experimental observation of either $K^{-1}K^{-1}$ or $K^{-1}K^{-1}V$ DCH still remains a challenging task, due to the comparatively low cross-sections of these processes. The intense short pulses produced by an XFEL have been shown to be a solution to this problem, by allowing for multi-photon absorption, but the XFEL sources are significantly less common than SR sources, which in combination with the high demand of the former for other scientific purposes, has resulted in a very limited number of DCH works [80, 81]. The development of an improved experimental setup which will overcome the limitations associated with the observation of ts-DCH states,

would lead us to a deeper understanding of the mechanisms causing the creation of such states, and would allow for ts-DCH spectroscopy to be established as a standard technique augmenting conventional ESCA. The application of this highly sensitive technique in small molecules and biomolecules is expected to have a significant impact on the fields of chemistry and biology, enhancing our understanding of chemical and biological processes.

Furthermore, new physical insight can be gained from the decay patterns of DCH states. It is well known that the creation of an initial K-shell vacancy can result in an Auger cascade, potentially leading to the Coulomb explosion of the molecule. An antagonistic effect to the previous, in XFEL experiments, is the removal of the second K-shell electron, as the duration of the light pulse is comparable to the lifetime of the singly core-ionized state. X-ray coherent diffraction imaging (CDI) is a field where these processes are evident, and so a deeper understanding of both is crucial in order to correctly interpret the outcomes of such experiments.

Additionally, in what concerns the decay channels of DCH states, despite the fact that several works reporting on the hyper-satellite Auger structures due to their decay have been published, not much is known to date about the fluorescence decay of such states. X-ray emission spectroscopy (XES) is a powerful tool for probing the changes in the valence shell of a sample after a chemical reaction takes place, as demonstrated by M. Agåker *et al.* [82, 83] for the case of lithium halides. Conducting XES experiments after the creation of a double inner-shell vacancy might reveal new, hitherto unknown information on atoms and molecules.

Finally, performing DCH spectroscopy on surfaces and liquids is another challenging future task worth conducting. The motivation to perform such experiments, beyond the unravelling of the involved physical processes, is the use of solutions in several industrial domains asking for a more detailed understanding of their properties, as well as the vast number of chemical reactions taking place on surfaces and in aqueous solutions. An in depth understanding of the latter might have a crucial impact on our daily lives.

Acknowledgements

Having the opportunity to do a Ph.D between the University of Gothenburg and Sorbonne University was a great pleasure and honour for me and for that reason I would like first of all to thank my main supervisors, Professor Raimund Feifel from Gothenburg University and Dr. Marc Simon (DR) from Sorbonne University (LCP-MR), for giving me the opportunity to do my Ph.D as a part of the Gothenburg-Paris collaboration, as well as for all their support throughout the duration of my doctoral studies .

I am deeply grateful to Dr. Ralph Püttner for his very important guidance since the beginning of this project, for being always there to answer every question that I had and for becoming informally a third supervisor of this work.

I would like to express my gratitude to Professor Maria Novella Piancastelli for all her critical comments and suggestions on this project. Furthermore, I wish to thank Professor Stéphane Carniato for his theoretical support which was crucial for the interpretation of the experimental outcomes of this work.

For the numerous and fruitful beamtimes in SOLEIL, as well as for a very nice work environment during my stay in Paris, I want to thank all the members of the Paris group, Professor Loïc Journel, Oksana Travnikova, Tatiana Marchenko, Renauld Guillemin, Iyas Ismail and Gildas Goldsztejn. My sincere thanks to Denis Céolin for his valuable support in every beamtime at GALAXIES.

From the Gothenburg group I wish to thank Andreas and Richard, with whom I started to work with since I was a master student, for the nice moments inside and outside work (and for helping carry my furniture...) and of course all the members of the group, Jonas, Omid, Måns and Vasyl. I am also thankful to my fellow Ph.D students from the Paris group, Jessica, Farzad, Mostafa and Nacer, it was a pleasure guys.

One should not forget of course the help that people from the human resources offer when it comes to administrative issues, for that reason I would like to thank Maria Siirak, Clara Wilow Sundh and Pernilla Larsson from Gothenburg University, and David Massot from Sorbonne University.

Last but not least, I want to thank my family for their support all these years that I have spent away from them, for always believing in me and for always setting a good example for me. I couldn't have done it without you!

References

[1] E. Rutherford, Philosophical Magazine **21**, Series 6, 669-688 (1911)

[2] J.J. Thomson, Philosophical Magazine **7**, 39 237-265 (1904)

[3] N. Bohr, Philosophical Magazine **26**, 151 1-24 (1913)

[4] L. De Broglie, *Recherches sur la théorie des quanta*, Doctoral thesis at Faculty of Science, University of Paris (1924), Ann. de Physique **3**, 22 (1925)

[5] E. Schrödinger, Physical Review **28**, 6 1049-1070 (1926)

[6] F. Jensen, *Introduction to Computational Chemistry*, John Willey and Sons Ltd, 2nd Edition, 2007

[7] A. Einstein, Ann. der Physik **332**, 132 (1905)

[8] H. Hertz, Ann. der Physik **267**, 983 (1887)

[9] K. Siegbahn, Nova Acta Regiae Soc. Sci. Upsal. **20** (1967)

[10] D.W. Turner & M.I.A. Jobory, J. Chem. Phys. **37**, 3007 (1962)

[11] K. Siegbahn, *ESCA Applied to Free Molecules*, Noth Holland Pub., 1970

[12] L.S. Cederbaum, F. Tarantelli, A. Sgamellotti & J. Schirmer, J. Chem. Phys. **85**, 6513 (1986)

[13] S. Carniato *et al.*, J. Chem. Phys. **142**, 014307 (2015)

[14] S. Carniato *et al.*, J. Chem. Phys. **142**, 014308 (2015)

[15] H. Ågren *et al.*, J. Electron Spectrosc. Relat. Phenom. **14**, 27 (1978)

[16] M.N. Piancastelli, Eur. Phys. J. Special Topics **222**, 2035-2055 (2013)

[17] J.J. Sakurai, *Modern Quantum Mechanics*, Revised Edition, Addison Wesley, 1994

[18] P. Atkins & R. Friedman, *Molecular Quantum Mechanics*, Fifth Edition Oxford University Press, 2011

[19] P. Atkins & J. De Paula "*Atkins' Physical Chemistry*", Ninth Edition, Oxford University Press, 2010

[20] M. Born & J.R. Oppenheimer, Ann. der Physik **389**, 457 (1927)

[21] T. Koopmans, Physica **1**, 104 (1934)

[22] M. Tashiro *et al.*, J. Chem Phys. **132**, 184302 (2010)

[23] O. Takahashi *et al.*, J. Phys. Chem. A **115**, 12070 (2011)

[24] B.H. Bransden & C.J. Joachain, *Physics of Atoms and Molecules*, Second Edition, Pearson Education, 2003

[25] T. Åberg, Phys. Rev. **156**, 35 (1967)

[26] M. Abramowitz & I.A. Stegun, *Handbook of Mathematical functions with Formulas, Graphs and Mathematical Tables*, Tenth Edition, United States Department of Commerce, National Bureau of Standards, 1972

[27] J. Franck, Transaction of the Faraday Society **21**, 536 (1926)

[28] E. Condon, Phys. Rev. **28**, 1182 (1926)

[29] G. Herzberg, *Molecular Spectra and Molecular Structure I. Spectra of Diatomic Molecules*, Van Nostrand, New York 1950

[30] J.H.D. Eland *et al.*, Phys. Rev. Lett. **105**, 213005 (2010)

[31] P. Lablanquie *et al.*, Phys. Rev. Lett. **106**, 063003 (2011)

[32] M. Nakano *et al.*, Phys. Rev. Lett. **111**, 123001 (2013)

[33] R. Püttner *et al.*, Phys. Rev. Lett. **114**, 093001 (2015)

[34] G. Goldsztejn *et al.*, Phys. Rev. Lett. **117**, 133001 (2016)

[35] P. Lablanquie *et al.*, Phys. Rev. Lett. **107**, 193004 (2011)

[36] M. Nakano *et al.*, Phys. Rev. Lett. **110**, 163001 (2013)

[37] P. Linusson *et al.*, Phys. Rev. A **83**, 022506 (2011)

[38] T.D. Thomas, Phys. Rev. Lett. **52**, 417 (1984)

[39] R.L. Martin & D.A. Shirley, J. Chem. Phys. **64**, 3685 (1976)

[40] V.G. Yarzhemsky & M. Ya. Amusia, Phys. Rev. A **93**, 063406 (2016)

[41] D. Atwood, *Soft X-RAYS AND EXTREME ULTRAVIOLET RADIATION, Principles and Applications*, Cambridge University Press 1999

[42] J.-P. Rueff *et al.*, J. Synchrotron Radiat. **22**, 175 (2015)

[43] https://www.synchrotron-soleil.fr/fr/lignes-de-lumiere/galaxies

[44] D. Céolin *et al.*, J. Electron Spectrosc. Relat. Phenom. **190**, 188 (2013)

[45] T.J.M. Zouros & E.P. Benis, J. Electron Spectrosc. Relat. Phenom. **125**, 221 (2002)

[46] F.H. Read *et al.*, J. Electron Spectrosc. Relat. Phenom. **4**, 293 (1974)

[47] NIST Atomic Spectra Database

[48] G.C. King, M. Tronc, F.H. Read & R.C. Bradford, J. Phys. B: At. Mol. Phys. **10**, 2479 (1977)

[49] M. Breinig *et al.*, Phys. Rev. A **22**, 520 (1980)

[50] J.H.D. Eland *et al.*, Phys. Rev. Lett. **90**, 053003 (2003)

[51] G. Beamson, H.Q. Porter & D.W. Turner, J. Phys. E: Sci. Instrum. **13**, 64 (1980)

[52] E. Andersson, *Multi-Electron Coincidence Studies of Atoms and Molecules*, Dissertation publicly defended at Uppsala University, 2010

[53] S. Plogmaker *et al.*, Rev. Sci. Instrum. **83**, 013115 (2012)

[54] S. Carniato *et al.*, Phys. Rev. A **94**, 013416 (2016)

[55] R. Püttner *et al.*, Phys. Rev. A **83**, 043404 (2011)

[56] J. Stöhr, *NEXAFS Spectroscopy*, Springer Series in Surface Science 1992

[57] C.J. Foot, *Atomic Physics*, Oxford University Press 2005

[58] D.B. Beach *et al.*, J. Am. Chem. Soc. **106**, 536 (1984)

[59] T.D. Thomas, J. Phys. Chem. A **116**, 3856 (2012)

[60] K. Ueda & O. Takahashi, J. Electron Spectrosc. Relat. Phenom. **185**, 301 (2012)

[61] N. Kryzhevoi, M. Tashiro, M. Ehara & L.S. Cederbaum, J. Chem. Phys. **137**, 154316 (2012)

[62] M.N. Piancastelli, D.W. Lindle, T A. Ferrett & D.A. Shirley, J. Chem. Phys. **86**, 2765 (1987)

[63] F. Sette, J. Stöhr & A.P. Hitchcock, J. Chem. Phys. **81**, 4906 (1984)

[64] M.N. Piancastelli, J. Electron Spectrosc. Relat. Phenom. **100**, 167 (1999)

[65] A.P. Hitchcock, M. Tronc & A. Modelli, J. Phys. Chem. **93**, 3068 (1989)

[66] G.R. Wight & C.E. Brion, J. Electron Spectrosc. Relat. Phenom. **4**, 335 (1974)

[67] A.P. Hitchcock and C.E. Brion, J. Electron Spectrosc. Relat. Phenom. **18**, 1 (1980)

[68] S. Carniato *et al.* Supplementary material of Ref. [14] at https://aip.scitation.org/doi/suppl/10.1063/1.4904274

[69] T.K. Sham, B.X. Yang, J. Kirz & J.S. Tse, Phys. Rev. A **40**, 652 (1989)

[70] G.R. Wight & C.E. Brion, J. Electron Spectrosc. Relat. Phenom. **3**, 191 (1974)

[71] S. Carniato, J. Chem. Phys. **126**, 224307 (2007)

[72] L. Inhester, C.F. Burmeister, G. Groenhof & H. Grubmüller, J. Chem. Phys. **136**, 144304 (2012)

[73] O. Takahashi, N. Kunitake & S. Takaki, J. Phys. B: At., Mol., Opt. Phys. **48**, 204001 (2015)

[74] M. Odelius *et al.*, Phys. Rev. Lett. **94**, 227401 (2005)

[75] A. Nilsson, S. Schreck, F. Perakis & L.G.M. Pettersson, Adv. Phys.: X **1**, 226 (2016)

[76] T. Marchenko *et al.*, Phys. Rev. Lett. **119**, 133001 (2017)

[77] O. Travnikova *et al.*, Phys. Rev. Lett. **116**, 213001 (2016)

[78] O. Travnikova *et al.*, Phys. Rev. Lett. **118**, 213001 (2017)

[79] G. Goldsztejn *et al.*, Phys. Rev. A **96**, 012513 (2017)

[80] N. Berrah *et al.*, Proc. Natl. Acad. Sci. U.S.A **108**, 16912 (2011)

[81] P. Salén *et al.*, Phys. Rev. Lett. **108**, 153003 (2012)

[82] M. Agåker *et al.*, Phys. Rev. Lett. **93**, 016404 (2004)

[83] M. Agåker & J.E. Rubensson, Phys. Rev. B. **75**, 045112 (2007)